BỘ GIÁO DỤC VÀ ĐÀO TẠO
TRƯỜNG ĐẠI HỌC CÔNG NGHỆ KỸ THUẬT
THÀNH PHỐ HỒ CHÍ MINH

PHAN THANH VŨ

NGHIÊN CỨU PHÁT TRIỂN CƠ CẤU ĐÀN HỒI ỔN ĐỊNH MÔ-MEN CHO CÁC ỨNG DỤNG TRONG CƠ SINH HỌC

CÔNG TRÌNH NGHIÊN CỨU
LUẬN ÁN TIẾN SĨ
NGÀNH: KỸ THUẬT CƠ KHÍ - 9520103

Tp. Hồ Chí Minh, tháng năm 2026

MỤC LỤC

Mechanism and Machine Theory 215 (2025) 106179

Contents lists available at ScienceDirect

Mechanism and Machine Theory

journal homepage: www.elsevier.com/locate/mechmt

Research paper

Robust design and optimization of a large-stroke compliant constant-torque mechanism under fabrication uncertainties

Thanh-Vu Phan [a], Van Men Truong [b], Huy-Tuan Pham [a,*], Van-Khien Nguyen [c], Amina Bukayeva [d]

[a] Faculty of Mechanical Engineering, Ho Chi Minh City University of Technology and Education, 01 Vo Van Ngan street, Thu Duc city, Ho Chi Minh City, Vietnam
[b] School of Engineering and Technology, Tra Vinh University, 126 Nguyen Thien Thanh street, Ward 5, Trà Vinh 87000, Vietnam
[c] Faculty of Mechanical Engineering and Technology, Ho Chi Minh City University of Industry and Trade, 140 Le Trong Tan Street, Tay Thanh Ward, Tan Phu District, Ho Chi Minh City, Vietnam
[d] Caspian University of Technologies and Engineering named after Sh. Yessenov, Microdistrict 32, Aktau 130000, Kazakhstan

ARTICLE INFO

Keywords:
Constant-torque mechanism
Large stroke
Genetic algorithm
Chained beam-constraint model
Reliability-based optimization

ABSTRACT

Compliant constant-torque mechanisms (CCTMs) are capable of delivering a stable output torque across a wide range of input rotational angles. Owing to their compact design and structural simplicity, they offer an attractive alternative to complex active control systems and have gained considerable research attention in recent decades. In many cases, particularly those involving large-stroke applications, CCTMs are fabricated from thin flexure beams using conventional subtractive machining methods, which makes them vulnerable to fabrication-induced variations that may compromise performance. This study presents an integrated design and optimization framework that explicitly accounts for fabrication uncertainties, enhancing the reliability of large-stroke CCTMs. By combining the Chained Beam-Constraint Model, the First-Order Reliability Method, and the Non-dominated Sorting Genetic Algorithm II, a reliability-based design optimization procedure is established. The optimized CCTM demonstrates a constant torque range up to 88°, an average torque deviation within 3%, and a reliability of 99.88%. Theoretical analyses, finite element simulations, and experimental validation confirm the framework's effectiveness in delivering robust and high-performance CCTMs suitable for precision applications.

1. Introduction

Compliant mechanism (CM) and its special categories such as bistable mechanisms [1], multi-stable mechanisms [2], constant force mechanisms (CFMs) [3], and constant torque mechanisms (CTMs) [4] exhibit remarkable characteristics inherent to CMs, including simplicity, lightweight, mobility, and precision. Bistable mechanisms and multi-stable mechanisms are known for their ability to maintain multiple stable positions, making them ideal for applications requiring discrete positional control. CFMs provide a consistent force over a range of displacements, which is beneficial in applications like force sensors and actuators [5]. Among these, CTMs are particularly valuable due to their ability to deliver a constant torque over a range of motion. However, designing CTMs remains challenging, primarily because of limitations in their achievable rotation range. Despite this, CTMs have been widely utilized in

* Corresponding author.
E-mail address: phtuan@hcmute.edu.vn (H.-T. Pham).

https://doi.org/10.1016/j.mechmachtheory.2025.106179
Received 20 March 2025; Received in revised form 9 August 2025; Accepted 11 August 2025

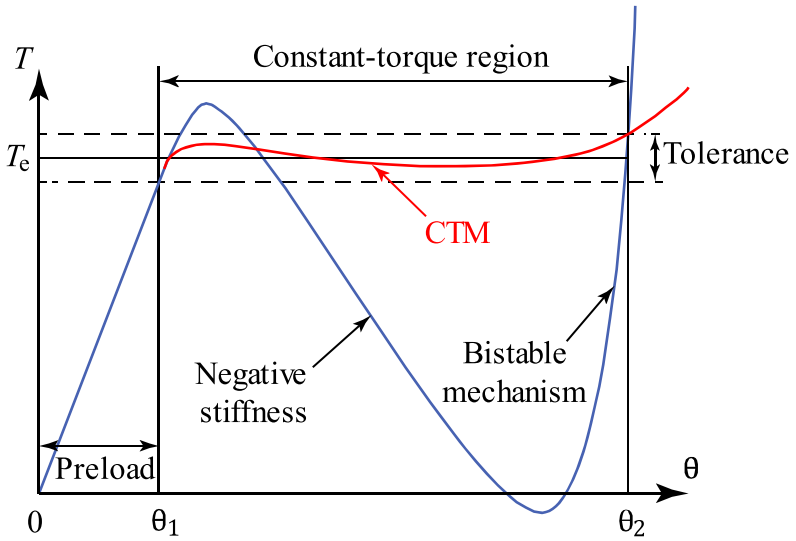

Fig. 1. Torque – angle curve of a constant-torque mechanism.

various applications, demonstrating their versatility and importance in the field of compliant mechanism design. Common applications of CTMs include assistive devices [6,7], constant-force grippers [8], medical instruments [9] and torsional vibration isolators [10].

Despite their potential, the design of CTMs remains challenging, especially for achieving large-stroke performance while maintaining torque constancy. Two dominant design strategies have emerged: stiffness combination methods [10–13] and optimized beam profiles [14–16]. While several "large-stroke" CTMs have been proposed [17–19], they commonly exhibit preload regions that precede the constant-torque phase, thereby limiting their effectiveness. Pre-compressed beams have been introduced to address this issue [12,20,21], yet these solutions have not eliminated the key limitations.

From previous studies, it is evident that most large-stroke CCTMs rely on optimal curve beams for their design. Despite advances in this area, a closer examination of existing literature reveals three persistent and interrelated challenges that hinder further advancements in large-stroke CTM design: (1) nonlinear torque modeling under large deformations, (2) material performance under large strain, and (3) fabrication-induced uncertainties.

First, accurate and efficient computational models are essential for simulating and optimizing the rotation-torque behavior. Although several techniques exist [22], many are computationally expensive or insufficiently accurate for complex geometries. Among them, the chained beam-constrained model (CBCM) has been proven to provide both simplicity and accuracy in modeling large deformations of straight beams [23], arc-curved beams [24], and arbitrary curved beams [25]. Additionally, CBCM offers a significant reduction in computation time compared to nonlinear finite element analysis (FEA) method [23,25,26], making it an ideal candidate for iterative optimization.

Second, due to the large deformation experienced by CCTMs, selecting appropriate materials is crucial. According to the literature, polymers are generally considered the most suitable material for this type of mechanism. However, a polymer with a low elastic modulus can lead to a reduced output torque, limiting the practical applications of the mechanism. Among available polymers, polyether ether ketone (PEEK) has been widely adopted in the design of large-stroke CCTMs because of its favorable mechanical properties [17–19,27]. In this study, PEEK is selected as the primary material for CCTM fabrication.

Third, although PEEK offers excellent mechanical and thermal properties, achieving precise flexure beam geometries from this material is nontrivial. Due to the substantial deformation characteristics required in CCTMs, slender flexure beams typically require a width of less than 0.7 mm and an out-of-plane thickness of at least 5.0 mm to ensure their performance [17,27,28]. Conventional manufacturing methods struggle with the thin, high-aspect-ratio features required for in-plane bending. CNC milling, though common, introduces random errors due to cutting forces, leading to shape distortions and variations in beam width between designed and fabricated geometries [12,17,19,27,28]. These deviations often push designs beyond acceptable performance limits.

Current deterministic optimization approaches do not explicitly consider such uncertainties. As a result, designs may lie perilously close to unsafe boundaries, rendering them unreliable under real-world conditions. To address this problem, it is essential to adopt a design framework that explicitly accounts for uncertainties and ensures that optimal solutions reside well within the safety domain. Reliability-based design optimization (RBDO) frameworks incorporate probabilistic constraints, ensuring that optimized designs are robust against manufacturing-induced variations. Surprisingly, despite their relevance, RBDO methods have not been integrated into CTM design. This omission represents a significant research gap.

Various approaches have been proposed to solve reliability analysis problems, with the most commonly used methods including the First Order Reliability Method (FORM), the Second Order Reliability Method (SORM) [29] and Monte Carlo Simulation (MCS) [30]. Among these, MCS, while accurate, demands significant computational resources, rendering its impractical for complex, multi-variable problems such as the optimization of CCTMs. Considering the trade-off between computational efficiency and accuracy,

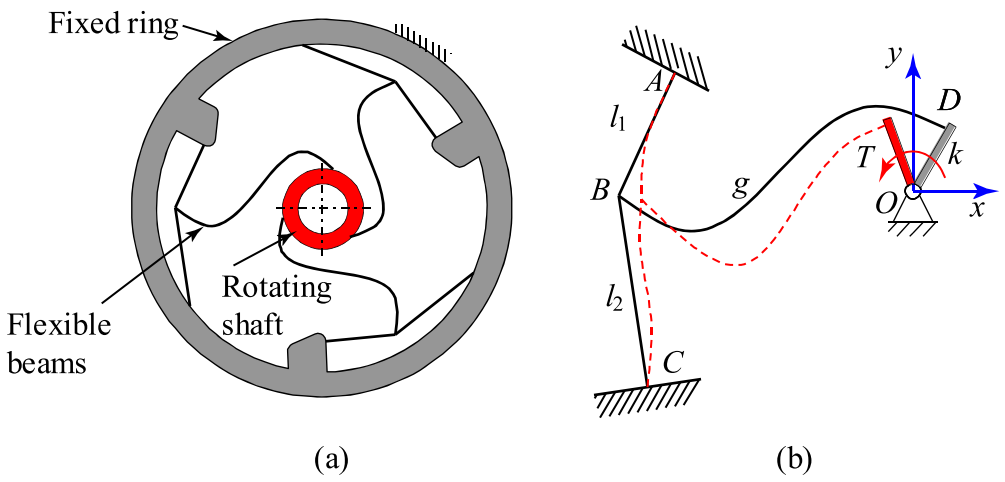

Fig. 2. CCTM concept of (a) complete structure and (b) one branch.

FORM is selected for the reliability analysis in this research. Furthermore, to integrate reliability analysis with optimization and establish a comprehensive RBDO framework, three main strategies have been proposed: Double Loop Method (DLM) [31], Decouple Double Loop Method (DDLM) also known as Sequential Optimization and Reliability Assessment (SORA) [32], and Single Loop Deterministic Method (SLDM) [33]. Among these approaches, DLM is chosen in this study due to its ability to directly incorporate reliability constraints within the optimization algorithm, simplifying implementation and enhancing the integration of reliability considerations into the design process.

This study addresses the mentioned research gap by proposing a multi-objective RBDO framework for the design of large-stroke CTMs fabricated from PEEK. The framework incorporates shape and size deviations of flexure beams due to machining errors. CBCM is used for efficient kinetostatic analysis. FORM is employed for reliability evaluation due to its balance of accuracy, and efficiency and the optimization is performed using NSGA-II, with reliability constraints integrated via the DLM method, to ensure robust and feasible designs. The result is a novel CTM design that achieves a large angular stroke of up to 88^o within a compact footprint while explicitly accounting for manufacturing uncertainties. This work not only advances the state of CTM design but also introduces a generalized methodology for reliability-based optimization in compliant mechanisms.

2. Design and optimization

2.1. Design concept

A CCTM is designed to deliver a nearly constant torque over a specified range of motion, as illustrated in Fig. 1. At the onset of operation, the rotational angle increases from 0 to θ_1, resulting in a gradual rise in torque which is referred to as the preload stage. Subsequently, as the angle continues to increase from θ_1 to θ_2, the torque remains approximately constant around the target value T_e. This phase is defined as the constant-torque stage. Within this range, the torque may fluctuate slightly around the target value but remains within the allowable tolerance, thereby enabling the identification of the two characteristic points θ_1 and θ_2 on the torque-angle response curve. While the torque magnitude can vary within defined limits to meet specific design objectives, maintaining this characteristic can be challenging due to uncertainties arising during fabrication. To address these challenges, this research integrates RBDO to ensure the robust performance of the CCTM, accounting for variations in the manufacturing process that may otherwise compromise its constant torque behavior.

As illustrated in Fig. 1, the proposed CCTM in this study is inspired by bistable mechanisms (BMs). BMs are typically constructed from curved beams [34], in which a negative stiffness region is located between two regions of positive stiffness. By integrating these curved beams with additional flexural elements that compensate for the negative stiffness region and bring the overall stiffness to zero, a CCTM can be obtained. To accomplish this, one end of the curved beam is connected to two straight beams to adjust the original negative stiffness region of the BM, as shown in Fig. 2(b). The CCTM configuration proposed in this research comprises three symmetrically arranged compliant branches positioned between a rigid outer ring and a rotating inner shaft, as depicted in Fig. 2(a). Each branch consists of three flexural elements, shown in Fig. 2(b): a curved beam *g*, which serves as the primary deforming component, and two straight beams, l_1 and l_2, which function as flexural pivots to minimize stress concentrations and enhance overall structural integrity. This configuration is conceptually analogous to Bai's parallel-guided compliant mechanism [17], which employs a similar approach to alleviate axial loading on their main straight beam. However, the inclusion of a curved beam in conjunction with two straight beams in the present design introduces additional degrees of freedom and design flexibility, enabling the development of mechanisms with a broader constant torque working range and a more compact structure.

Structurally, one end of each straight beam is anchored to the rigid outer ring at points *A* and *C*. The three flexural elements intersect at point *B*, forming a critical junction in the compliant branch. The free end of the curved beam *g* connects to a rigid link *k* at

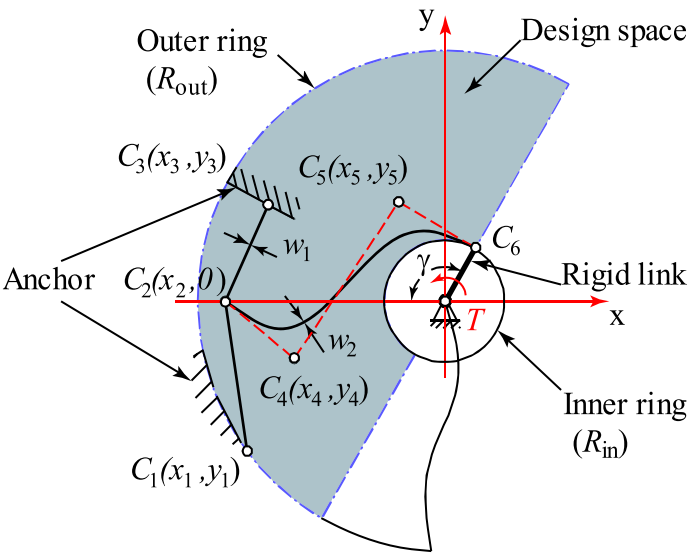

Fig. 3. Design parameters of the CCTM.

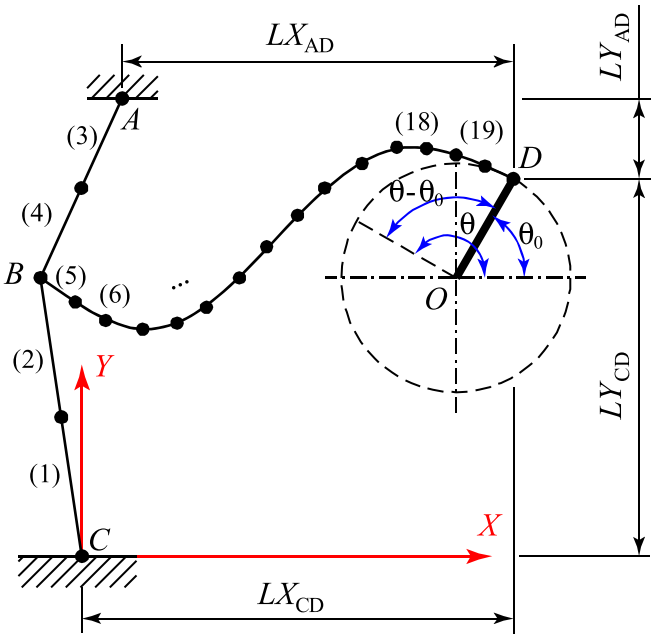

Fig. 4. Parameters used for modeling.

point D, which simultaneously serves as the rotating shaft in the complete mechanism (Fig. 2(a)). When an external torque T is applied to the rigid link k, causing rotation about point O, the flexural elements deform accordingly. After surpassing an initial preload region, the mechanism produces a torque output that remains nearly constant over a designated range of rotation angles, known as the constant torque working range.

2.2. Kinetostatic model

Due to the symmetrical configuration, only one branch is used for kinetostatic analysis, as shown in Fig. 3. The flexible beams have uniform width values, where w_1 and w_2 are the widths of the straight and curved beams, respectively. All three beams have equal and uniform thickness t throughout their lengths. The lower straight beam (l_2) passes through two points $C_1(x_1, y_1)$ and $C_2(x_2, y_2)$, while the upper straight beam (l_1) passes through two points $C_2(x_2, y_2)$ and $C_3(x_3, y_3)$. The curved beam (g) is a cubic Bezier curve which is

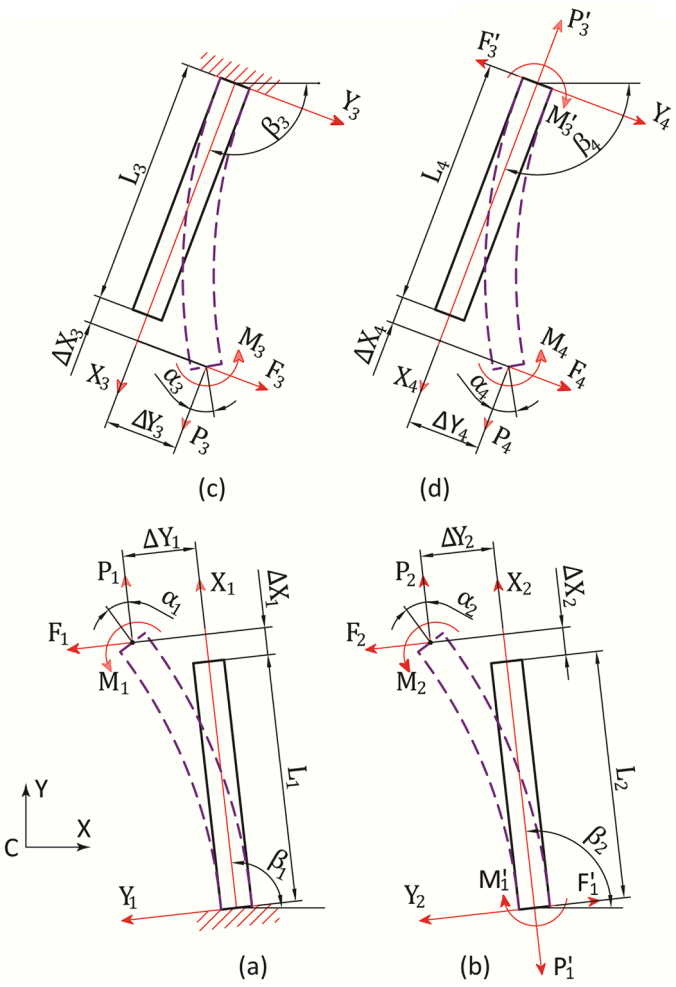

Fig. 5. Free body diagram of (a) element 1, (b) element 2, (c) element 3, (d) element 4.

parameterized by four control points $C_2(x_2, y_2)$, $C_4(x_4, y_4)$, $C_5(x_5, y_5)$, and $C_6(x_6, y_6)$ follows as. To achieve the desired design objectives, the configuration's shape and size must be adjusted within the design space by modifying fifteen design variables (DVs), including the twelve coordinates of points C_1 to C_6 and three variables w_1, w_2, t. However, to reduce computation time by minimizing the number of DVs, point C_2 is constrained to the horizontal centerline, setting its coordinates to $(x_2, 0)$. Additionally, point C_6 is fixed on the inner ring of radius R_{in} and is determined by the angle γ. The radius R_{in} is constrained to be sufficiently large to serve as the rotating shaft of the mechanism. Consequently, point $C_6(x_6, y_6)$ coordinates are re-parameterized as $(R_{in}sin\gamma,\ R_{in}cos\gamma)$. Since the thickness t influences only the magnitude of the torque without altering the characteristics of the torque graph, it is not chosen as a DV. As a result, the model retains thirteen DVs: the coordinates $x_1,\ y_1, x_2, x_3, y_3, x_4, y_4, x_5, y_5$, the radius R_{in}, the angle γ and the uniform widths w_1, w_2, as illustrated in Fig. 3.

Due to the significant advantages outlined in the introduction, CBCM has been used to model the CCTM to calculate the relationship among rotation, torque, and stress [23]. To facilitate the model description, the ends of beams are labeled A, B, C, and D, as shown in Fig. 4, similar to Fig. 2. These three beams intersect at point B, while points A and C are fixed. Point C is chosen as the origin of the global coordinate system XCY. According to the results of a convergence study, the straight beams AB and BC are divided into two elements each, while the curved beam BD is divided into 15 elements. Thus, beam BC consists of elements 1 and 2, beam AB consists of elements 3 and 4, and beam BD consists of elements 5 through 19.

As shown in Figs. 5 and 6, after releasing the link, we apply the transverse force F_i, axial force P_i and moment M_i to elements 1, 2, 3, 4, and 5 along with the local coordinate system $O_iX_iY_i$ attached to each element $(i = 1, 2, \ldots, 5)$. Each local coordinate system creates an angle β_i with the global coordinate system XCY. The displacements in the X_i and Y_i directions are ΔX_i and ΔY_i, respectively. The rotational deformation angle of the i^{th} element, measured relative to its initial position in the direction of the X_i axis, is denoted as α_i. The length of each element measured along the X_i axis is denoted as L_i. We derive the expressions from (1) to (9) according to the static equilibrium condition.

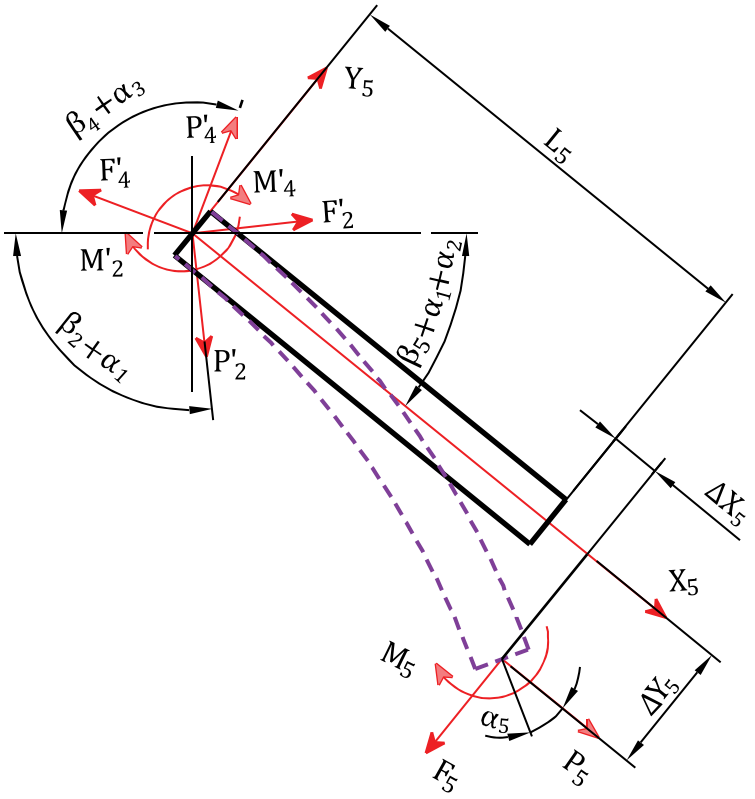

Fig. 6. Free body diagram of the element 5.

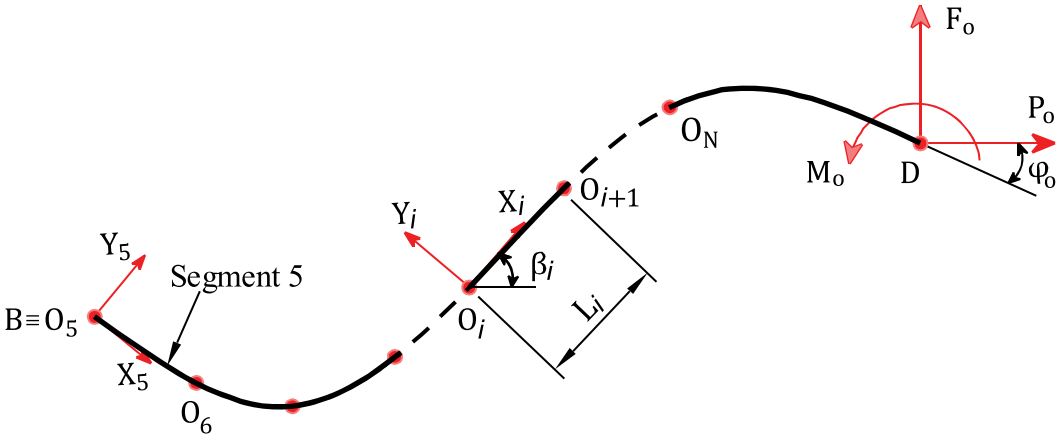

Fig. 7. Discretization for the curved beam.

$$P_1 = P_2\cos\alpha_1 - F_2\sin\alpha_1 \tag{1}$$

$$F_1 = F_2\cos\alpha_1 + P_2\sin\alpha_1 \tag{2}$$

$$M_1 = M_2 + F_2(L_2 + \Delta X_2) - P_2\Delta Y_2 \tag{3}$$

$$P_3 = P_4\cos\alpha_3 - F_4\sin\alpha_3 \tag{4}$$

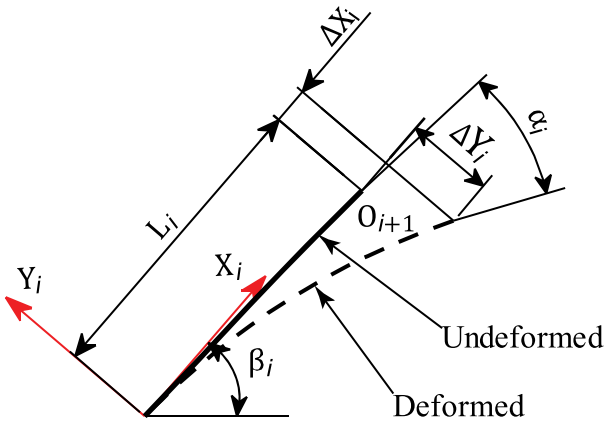

Fig. 8. The i^{th} element of the curved beam.

$$F_3 = F_4\cos\alpha_3 + P_4\sin\alpha_3 \tag{5}$$

$$M_3 = M_4 + F_4(L_4 + \Delta X_4) - P_4\Delta Y_4 \tag{6}$$

$$P_2\cos(\beta_2+\alpha_1) - F_2\sin(\beta_2+\alpha_1) + P_4\cos(\beta_4+\alpha_3) - F_4\sin(\beta_4+\alpha_3) + P_5\cos(\beta_5+\alpha_1+\alpha_2) - F_5\cos(\beta_5+\alpha_1+\alpha_2) = 0 \tag{7}$$

$$-P_2\sin(\beta_2+\alpha_1) + F_2\cos(\beta_2+\alpha_1) + P_4\sin(\beta_4+\alpha_3) + F_4\cos(\beta_4+\alpha_3) + P_5\sin(\beta_5+\alpha_1+\alpha_2) + F_5\cos(\beta_5+\alpha_1+\alpha_2) = 0 \tag{8}$$

$$M_2 + M_4 - M_5 + P_5\Delta Y_5 - F_5(L_5 + \Delta X_5) = 0 \tag{9}$$

The angle between the rigid link OD and the horizontal axis at the initial position and the later position (deformed position of the CCTM) is denoted by θ_o and θ, respectively. Therefore, the displacement of the mechanism is the rotation angle ranging from 0 to $(\theta - \theta_o)$, as shown in Fig. 4.

The connection between the curved beam BD and the rigid link OD is released by applying forces F_o, P_o, and moment M_o at the endpoint D. The curved beam is divided into 15 elements (from element 5 to element 19), with each element with length L_i attached to a coordinate system $O_iX_iY_i$ located at its left end and forming an angle β_i with the global coordinate system, as shown in Fig. 7.

The static equilibrium equations between the 5^{th} element and the i^{th} elements ($i = 6, 7, \ldots, 19$) can be denoted in the matrix form, as shown in Eq. (10):

$$\begin{bmatrix} \cos(\varphi_i - \beta_5) & -sin(\varphi_i - \beta_5) & 0 \\ sin(\varphi_i - \beta_5) & cos(\varphi_i - \beta_5) & 0 \\ -\Delta Y_i & (L_i + \Delta X_i) & 1 \end{bmatrix} \begin{bmatrix} P_i \\ F_i \\ M_i \end{bmatrix} = \begin{bmatrix} P_5 \\ F_5 \\ M_{i-1} \end{bmatrix} \tag{10}$$

The rotational deformation angle of the i^{th} element, measured relative to its initial position, is denoted as α_i, as shown in Fig. 8. The slope φ_i of the i^{th} element after deformation, relative to the global coordinate system, is defined as follows:

$$\varphi_i = \beta_i + \sum_{k=5}^{i-1} \alpha_k \tag{11}$$

Force-displacement relationship of each element obtained from BCM [35]:

$$\begin{bmatrix} f_i \\ m_i \end{bmatrix} = \begin{bmatrix} 12 & -6 \\ -6 & 4 \end{bmatrix} \begin{bmatrix} \delta y_i \\ \alpha_i \end{bmatrix} + p_i \begin{bmatrix} 6/5 & -1/10 \\ -1/10 & 2/15 \end{bmatrix} \begin{bmatrix} \delta y_i \\ \alpha_i \end{bmatrix} + p_i^2 \begin{bmatrix} -1/700 & 1/1400 \\ 1/1400 & -11/6300 \end{bmatrix} \begin{bmatrix} \delta y_i \\ \alpha_i \end{bmatrix} \tag{12}$$

$$\delta x_i = \frac{t^2 p_i}{12L_i^2} - \frac{1}{2}\begin{bmatrix} \delta y_i & \alpha_i \end{bmatrix} \begin{bmatrix} 6/5 & -1/10 \\ -1/10 & 2/15 \end{bmatrix} \begin{bmatrix} \delta y_i \\ \alpha_i \end{bmatrix} - p_i \begin{bmatrix} \delta y_i & \alpha_i \end{bmatrix} \begin{bmatrix} -1/700 & 1/1400 \\ 1/1400 & -11/6300 \end{bmatrix} \begin{bmatrix} \delta y_i \\ \alpha_i \end{bmatrix} \tag{13}$$

in which the force parameters F_i, P_i, M_i and the deformation parameters ΔX_i, ΔY_i, α_i of the i^{th} element have been normalized as follows:

$$p_i = \frac{P_i L_i^2}{EI};\ f_i = \frac{F_i L_i^2}{EI};\ m_i = \frac{M_i L_i}{EI};\ \delta x_i = \frac{\Delta X_i}{L_i};\ \delta y_i = \frac{\Delta Y_i}{L_i};\ \alpha_i = \alpha_i \tag{14}$$

Where E is the Young's modulus of the material. The moment of inertia of the beam cross section is $I = tw^3/12$ with w is the in-plane

thickness of the beams (w_1 for the straight beams and w_2 for the curved beam).

Finally, geometric constraints must be added to the model to calculate the relationship between angular displacement and output torque. Let O be the rotational center of the mechanism, which is the center of the circle of radius R_{in}, and let A and C be fixed points. The distances OA and OC, when projected onto the X and Y directions of the global coordinate system, remain fixed regardless of whether the compliant elements are in their initial or deformed state. Therefore, the additional geometric constraint equations are as follows:

$$\sum_{i=5}^{n}\left[\begin{bmatrix} cos(\varphi_i+\alpha_3+\alpha_4) & -sin(\varphi_i+\alpha_3+\alpha_4) \\ cos(\varphi_i+\alpha_1+\alpha_2) & -sin(\varphi_i+\alpha_1+\alpha_2) \end{bmatrix}\begin{bmatrix} L_i(1+\Delta X_i) \\ L_i\Delta Y_i \end{bmatrix}\right]=\begin{bmatrix} LX_{AD}-R_{in}cos\theta_o+R_{in}cos\theta \\ LX_{CD}-R_{in}cos\theta_o+R_{in}cos\theta \end{bmatrix} \tag{15}$$

$$\begin{aligned} &L_3(1+\Delta X_3)sin\beta_3+L_3\Delta Y_3cos\beta_3+L_4(1+\Delta X_4)\sin(\beta_4+\alpha_3)+L_4\Delta Y_4\cos(\beta_4+\alpha_3) \\ &-\sum_{i=5}^{n}[sin(\varphi_i+\alpha_3+\alpha_4)L_i(1+\Delta X_i)+\cos(\varphi_i+\alpha_3+\alpha_4)L_i\Delta Y_i] \\ &=LY_{AD}+R_{in}sin\theta_o-R_{in}sin\theta \end{aligned} \tag{16}$$

$$\begin{aligned} &L_1(1+\Delta X_1)sin\beta_1+L_1\Delta Y_1cos\beta_1+L_2(1+\Delta X_2)\sin(\beta_2+\alpha_1)+L_2\Delta Y_2cos(\beta_2+\alpha_1) \\ &-\sum_{i=5}^{n}[sin(\varphi_i+\alpha_1+\alpha_2)L_i(1+\Delta X_i)+\cos(\varphi_i+\alpha_1+\alpha_2)L_i\Delta Y_i] \\ &=LY_{CD}-R_{in}sin\theta_o+R_{in}sin\theta \end{aligned} \tag{17}$$

$$\alpha_1+\alpha_2+\sum_{i=5}^{n}\alpha_i=\theta-\theta_o \tag{18}$$

$$\sum_{i=3}^{n}\alpha_i=\theta-\theta_o \tag{19}$$

From this, we can determine the reaction torque generated when an input rotation angle is applied, as expressed by the following equation:

$$T=F_oR_{in}cos(\theta-\alpha_1-\alpha_2-\varphi_{19})-P_oR_{in}sin(\theta-\alpha_1-\alpha_2-\varphi_{19})+M_o \tag{20}$$

where:

R_{in} is the radius of the inner ring or the length of rigid link OD.

LX_{AD}, LX_{CD}, LY_{AD}, and LY_{CD} are the distances of AD and CD, respectively, projected onto the X and Y directions of the global coordinate system in the undeformed state (Fig. 4) and are determined as follows:

$$LX_{AD}=LX_{BD}-LX_{AB} \tag{21}$$

$$LX_{CD}=LX_{BD}-LX_{CB} \tag{22}$$

$$LY_{AD}=LY_{AB}-LY_{BD} \tag{23}$$

$$LY_{CD}=LY_{CB}+LX_{BD} \tag{24}$$

Here, the symbols LX and LY represent the distances projected onto the X and Y directions of the global coordinate system in the undeformed state shown in Fig. 4 and are determined as follows:

$$LX_{CB}=L_1cos\beta_1+L_2cos\beta_2 \tag{25}$$

$$LY_{CB}=L_1sin\beta_1+L_2sin\beta_2 \tag{26}$$

$$LX_{AB}=L_3cos\beta_3+L_4cos\beta_4 \tag{27}$$

$$LY_{AB}=L_3sin\beta_3+L_4sin\beta_4 \tag{28}$$

$$LX_{BD}=\sum_{i=5}^{19}L_icos\beta_i \tag{29}$$

$$LY_{BD}=\sum_{i=5}^{19}L_isin\beta_i \tag{30}$$

where L_i is the length of the i^{th} element measured along the O_iX_i axis:

$$L_i = \sqrt{(x_{i+1} - x_i)^2 + (y_{i+1} - y_i)^2} \tag{31}$$

The rotation angles β_i of the local coordinate systems relative to the global coordinate system (relative to the OX axis):

$$\beta_i = arccos\left(\frac{|x_{i+1} - x_i|}{\sqrt{(x_{i+1} - x_i)^2 + (y_{i+1} - y_i)^2}}\right), (i = 1,\ 2,\ \ldots, 19) \tag{32}$$

The coordinates $x_i,\ y_i$ of the points on the curved beam BD are determined from the cubic Bezier curve equation with four control points $C_2,\ C_4,\ C_5$, and C_6:

$$P(t) = (1-t)^3 C_2 + 3t(1-t)^2 C_4 + 3t^2(1-t)C_5 + t^3 C_6 \tag{33}$$

in which $t \in [0,1]$. If the curve is divided into n elements, the value of t will be divided into steps of $1/n$. For $n = 15$, there are sixteen t-values between 0 and 1 with steps of 1/15. By substituting these values of t and the coordinates of the control points into Eq. (33), we obtain the coordinates (x_i, y_i) of the points on the curve, which are then used to calculate the angles and lengths based on Eqs. (31) and (32).

The normal stress of a single element is defined as follows:

$$\sigma(x) = \sigma_b(x) + \sigma_a \tag{34}$$

where $\sigma_b(x)$ is the bending stress at distance x from the origin of each segment and normalized by L_i, and σ_a is the tensile stress due to the axial force P

The bending stress at position x (occurring at the outermost fibers of the cross-section $w/2$) is obtained once the displacement ΔY_i is achieved [23]:

$$\sigma_b(x) = \frac{M(x)}{I}\frac{w}{2} = \frac{E\Delta Y_i'' w}{2L_i} \quad x \in [0;1] \tag{35}$$

where $M(x)$ is the internal bending moment at position x. $\Delta Y_i''$ is the curvature and is non-dimensionalized in CBCM (normalized by L_i). $\Delta Y_i''$ is defined for two cases:

for $p_i > 0,\ (r = \sqrt{p_i})$

$$\Delta Y_i'' = \frac{\tanh r\cosh(rx) - \sinh(rx)}{r} f_i + \frac{\cosh(rx)}{\cosh r} m_i \tag{36}$$

for $p_i < 0,\ (r = \sqrt{-p_i})$

$$\Delta Y_i'' = \frac{\tan r\cos(rx) - \sin(rx)}{r} f_i + \frac{\cos(rx)}{\cos r} m_i \tag{37}$$

The tensile stress is calculated as follows:

$$\sigma_a = \frac{|P_i|}{A} = E\frac{|p_i|w^2}{12{L_i}^2} \tag{38}$$

in which $A = wt$ is the cross-sectional area of the beam.

Thus, as a result of the calculation process using CBCM, the torque is obtained from Eq. (20) and the stress from Eq. (34).

2.3. Reliability-based NSGA-II optimization

This research aims to develop a CCTM with a maximized constant torque working range and minimized deviation between the generated and target torque, while ensuring reliable performance under manufacturing variability. In this study, the multi-objective optimization is performed using NSGA-II, with CBCM-based kinetostatic analysis and FORM-based reliability assessment. The NSGA-II algorithm was selected for its effectiveness in solving complex multi-objective nonlinear optimization problems, particularly through its non-dominated sorting and crowding distance mechanisms for maintaining solution diversity [36]. The optimization considers two objective functions: (1) maximizing the constant torque working range, as defined in Eq. (39), and (2) minimizing the deviation from the desired torque T_e, as given in Eq. (40)

$$Maximize(S) \tag{39}$$

with $S = \theta_2 - \theta_1$

Table 1
Formulation of the CCTM reliability-based optimization.

1. Objective functions: - Maximize the constant torque stroke according to Eq. (39) - Minimize the output torque deviation according to Eq. (40) 2. Limit state function (*): - $\{G(X_i) - D_0 \le 0\} \ge \Phi(\beta)$ (41) - With eight random variables: $\{X_i\} = \{x_2, y_2, x_4, y_4, x_5, y_5, w_1, w_2\}$ - Reliability $R \ge 99\%$
3. Design variables: - Coordinates of control points: $x_1, y_1, x_2, x_3, y_3, x_4, y_4, x_5, y_5$ - Beam widths: w_1, w_2 - Inner ring's radius: R_{in} - Initial angle of the rotating shaft: γ
4. Constraints: i. $g_1: 8 \le R_{in} \le 12$ (mm) ii $g_2: R_{in}^2 \le x_i^2 + y_i^2 \le R_{out}^2$ ($R_{out} \le 50$; $i = 1, 2, \ldots, 5$) iii $g_3: x_2 < x_4 < x_5$ iv $g_4: y_1 < 0 < y_3$ v. $g_5: \frac{\pi}{4} \le \gamma \le \frac{3\pi}{4}$ (rad) vi. $g_6: 0.5 \le w_i \le 1.0$ (mm) ($i = 1, 2$) vii. $g_7: 230 < T_e < 260$(Nmm) viii. Maximum stress, $g_8: \sigma_m < \sigma_y/\mathrm{SF}$ ix. Constant-torque stroke (degree): (*) $g_9: S - 70 \le 0$ x. Output torque deviation: (*) $g_{10}: \lvert T - T_e \rvert - 0.03T_e \le 0$

$$Minimize f(\theta) = \int_{\theta_1}^{\theta_2} (T - T_e)^2 d\theta \tag{40}$$

As shown in Fig. 1, θ_1 and θ_2 define the boundaries of the constant torque region. The desired constant torque value T_e is determined by taking the maximum torque value within a predefined range of initial rotation angles of the mechanism, set at 20^o. However, depending on the specific design configuration, the algorithm adjusts θ_1 and θ_2 so that the torque values $T(\theta_1)$ and $T(\theta_2)$ remain within $\pm 3\%$ of T_e. In addition, the selection of θ_1 and θ_2 must satisfy the constraint on the maximum value of the constant torque region. Therefore, these parameters are not predetermined for the optimization process.

The optimization problem is summarized in Table 1. Thirteen design variables as described in Section 2.2 are involved, subject to eight constraint functions, g_1 to g_8. These constraints control different aspects such as mounting space, branch geometry, rigid link angle, beam width, total torque range, and material stress limits. Function g_1 ensures sufficient space for mounting a shaft at the center of the mechanism. Function g_2 constrains the points from C_1 to C_5 to move freely within an annular region defined by the radii (R_{in}, R_{out}) and ensures that the outer diameter of the mechanism does not exceed 100 *mm*. Functions g_3 and g_4 constrain the control points to be in the desired order, avoiding creating infeasible designs. Function g_5 restricts the search range of the rigid link angle (γ), which determines point $C_6(R_{in}sin\gamma,\ R_{in}cos\gamma)$. Function g_6 constrains the uniform widths of the beams. Function g_7 controls the algorithm to search for CCTMs with overall T_e values, including three compliant branches, in the range of 230 – 260 (Nmm). Function g_8 ensures that the mechanism operates within the elastic range of the material, where the safety factor (SF) is 1.2. Besides the two objective functions and eight constraint functions used in the deterministic optimization introduced above, two additional limit state functions g_9 and g_{10} ensure the optimized CCTM achieves a working range greater than 70^o and an output torque deviation less than 3% from T_e with 99% reliability.

Based on prior experience with CCTMs, several key design parameters are selected as random variables for reliability analysis because of their sensitivity to the limit state functions. Among the three beams connected to form a branch of the structure, the curved beam plays the most critical role, primarily in deformation. However, point C_6, located on the inner circle, which is the rigid part of the structure, has minimal machining error. Furthermore, this point typically has little effect on the overall characteristics of CCTMs, so the values determining this point, including R_{in} and γ, are not chosen as random variables. Although the y-coordinate (y_2) of point C_2 is fixed at 0, this intersection point of the three beams significantly influences the shape of the entire structure. Therefore, it is treated as a random variable in the reliability analysis, with an average value of 0. The beam width primarily affects torque and stress values. However, when multiple beams are used to form a branch, as in this case, the correlation between beam widths significantly affects design objectives and reliability. Hence, the values w_1 and w_2 are also chosen as random variables.

With the above analysis, this reliability-based optimization problem has eight random variables, including the coordinates of points C_2, C_4, C_5 and two beam widths w_1, w_2. These variables follow normal distributions, with mean values (μ_i) equal to their design solutions and standard deviations (σ_i) derived from experimental data. Statistical analysis shows that the standard deviation (STD) σ can be approximately as $\sigma_i = 0.05$ *mm*. Therefore, this STD value has been applied to all random variables in the model. For an implicit and

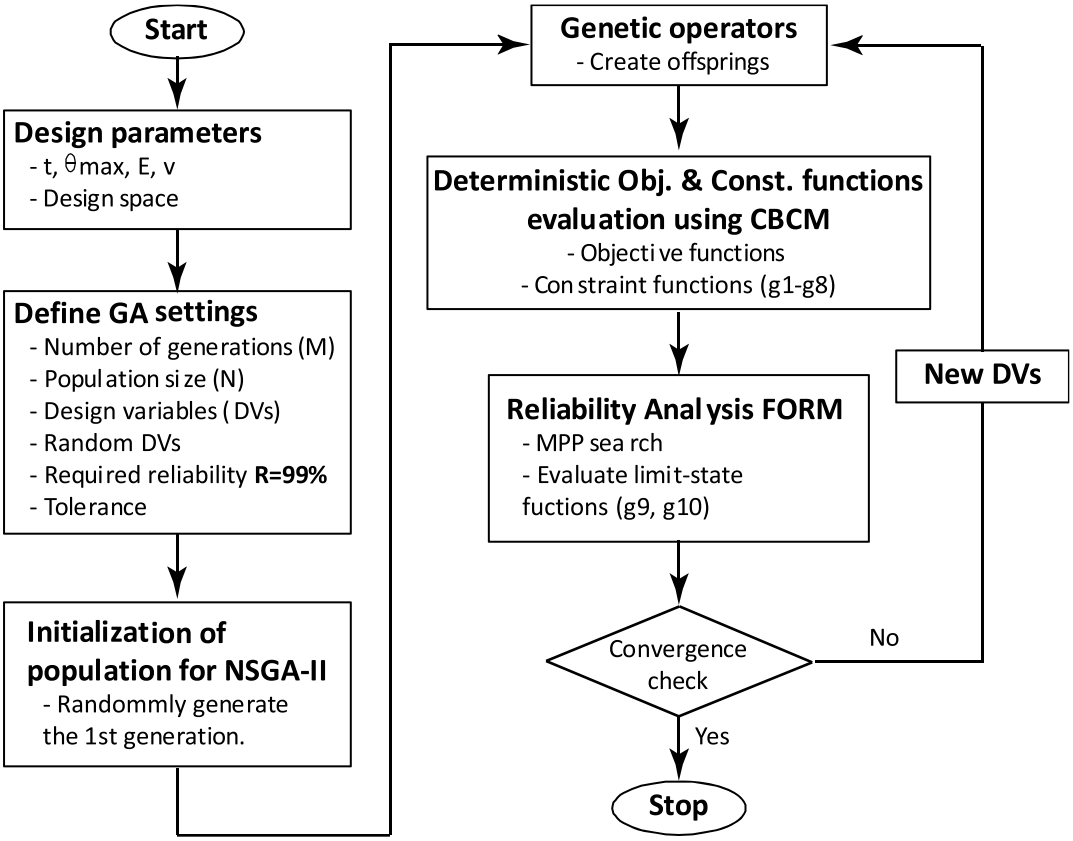

Fig. 9. The flowchart of the reliability-based optimization algorithm.

complex objective function like the one in this problem, suitable methods for the reliability analysis step include FORM, SORM, or MSC. However, FORM is employed for reliability analysis due to its computational efficiency.

The flowchart of the multi-objective reliability-based optimization algorithm is shown in Fig. 9. This process consists of two integrated steps performed automatically using MATLAB. The input parameters are predefined, including material properties, out-of-plane thickness, design space, and the maximum rotation angle of the mechanism. In addition, the GA parameters required for the algorithm to operate are shown in the "Define GA settings" box. First, using the preliminary input values, MATLAB randomly generates initial population with $N = 40$ candidates. The necessary condition for each design to be feasible if it satisfies the first eight constraints in Table 1 $(g_1 - g_8)$. Designs are then iteratively evolved using NSGA-II, with each iteration evaluating torque-rotation behavior via CBCM and reliability via FORM.

In each generation of evolution, after a set of optimal solutions are found by the Deterministic optimization block, each design point has thirteen DVs fulfilled the previous constraint functions $(g_1 - g_8)$. Next eight random variables $\{X_i\}$ from this design parameter set are further analyzed for reliability by considering the uncertainty of the input data via the Reliability analysis FORM block. This analysis step verifies the two last constraints (known as limit state functions) g_9 and g_{10} in Table 1. If these constraints are satisfied, the reliability index (β) will be calculated using the FORM method [30], ensuring that regardless of the uncertainty in the practical fabrication of the random variables, the optimum CCTM can still maintain its performance with 99% reliability.

Theoretically, the matrix procedure of FORM consists of the following steps [30]:

1. Formulate the two limit state functions, g_9 and g_{10}, which are implicit functions of the eight random variables $\{X_i\}$.
2. Set an initial design point $\{x_i^*\}$ of the random variables X_i (often choose mean values μ_i)
3. Determine the reduced variables $\{z_i^*\}$ corresponding to the design point $\{x_i^*\}$

$$z_i^* = \frac{x_i^* - \mu_{x_i}}{\sigma_{x_i}} \tag{42}$$

4. Determine the partial derivatives of the limit state functions with respect to the reduced variables using:

$$\{G\} = \{G_1\ G_2 \ldots G_8\}^T \tag{43}$$

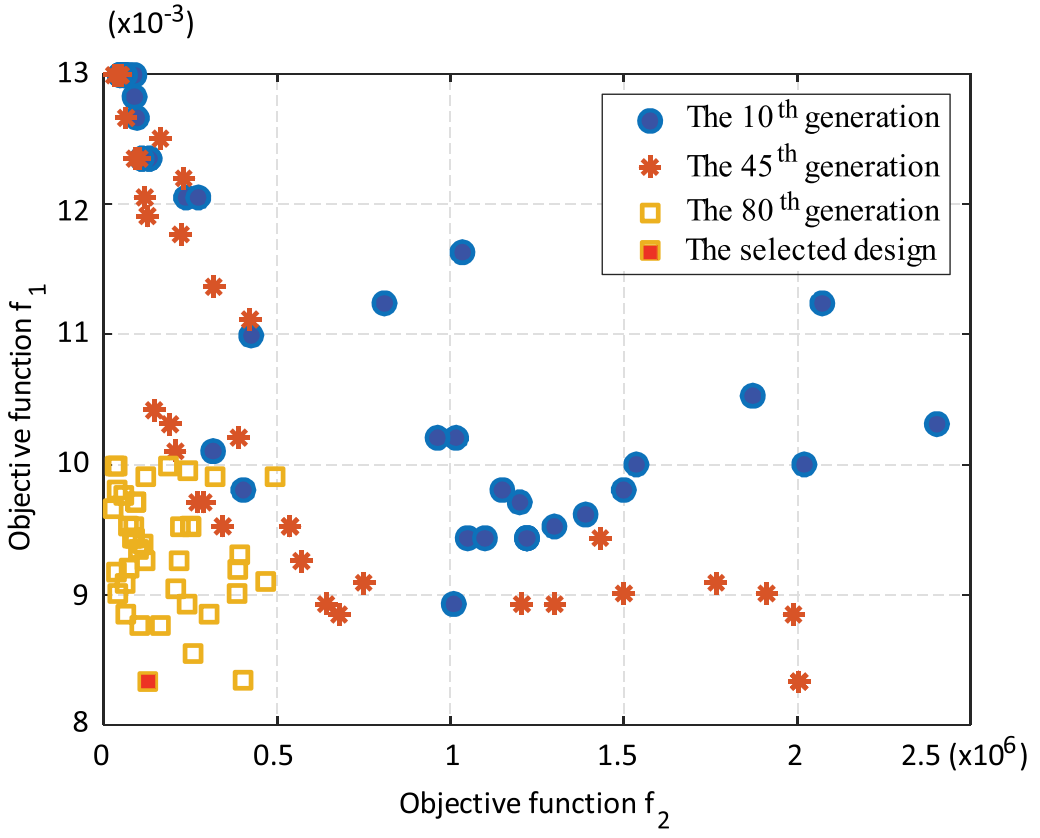

Fig. 10. Distribution of populations across generations during the evolutionary process.

where $G_i = \frac{\partial g_i}{\partial z_i}|_{evaluated\ at\ design\ point} = \frac{\partial g_i}{\partial x_i}\frac{\partial x_i}{\partial z_i} = \frac{\partial g_i}{\partial x_i}\sigma_{x_i}$

For the implicit functions, g_9 and g_{10}, we use the finite difference technique to calculate $\partial g_i/\partial x_i$ as:

$$\frac{\partial g_i}{\partial x_i} = \frac{g_i\left(x_i|_{evaluated\ at\ design\ point} + \Delta x_i\right) - g_i\left(x_i|_{evaluated\ at\ design\ point}\right)}{\Delta x_i}$$

5. Calculate an estimate of a reliability index β using the following formula:

$$\beta_{new} = \beta_{old} + \frac{g_i}{\sqrt{\{G\}^T\{G\}}} \tag{44}$$

6. Calculate a column vector containing the sensitivity factors using:

$$\{\alpha\} = \frac{\{G\}}{\sqrt{\{G\}^T\{G\}}} \tag{45}$$

7. Determine the new design point in reduced variable space for $n = 8$ random variables, using:

$$z_i^* = \alpha_i\beta_{new} \tag{46}$$

8. Determine the corresponding design point values in original coordinates for eight values in Step 7 using:

Table 2
Optimal values of design variables.

Design variables	Value	Unit
(x_1, y_1)	(-39.88, -15.42)	mm
x_2	-38.05	mm
(x_3, y_3)	(-30.58, 16.45)	mm
(x_4, y_4)	(-30.64, -14.36)	mm
(x_5, y_5)	(-8.63, 19.88)	mm
w_1	0.53	mm
w_2	0.60	mm
R_{in}	10.50	mm
γ	120	degree

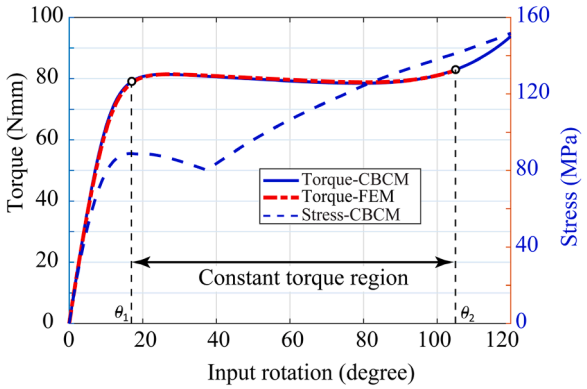

Fig. 11. Torque and stress results obtained from RBDO.

$$x_i^* = \mu_{x_i} + z_i^* \sigma_{x_i} \tag{47}$$

9. Repeat Steps 3 to 8 until β and the design point $\{x_i^*\}$ converge.

Finally, NSGA-II calculates the fitness value of each design to compare and rank them with other designs in the current generation. Offspring are generated using a specific type of crossover or mutation. Based on comparing crowding distance and non-dominated sorting, NSGA-II selects the most suitable individuals for the next generation. The algorithm terminates when one of the following conditions is met: 1) the evolution converges or the difference between two consecutive generations of the objective function is less than the tolerance; 2) the maximum number of generations of evolution (max_{iter}) is reached.

In this study, PEEK is selected as the material for the mechanism. For the isotropic and linear elastic models, Young's modulus (E) and Poisson's ratio (ν_p) of PEEK were taken as 3.58 GPa and 0.3, respectively. The thickness of the mechanism was chosen to be 10.0 mm.

3. Results and discussion

3.1. Optimization results

The evolutionary process converged after 80 generations. The population distribution of several selected generations is illustrated in Fig. 10. Using the proposed RBDO optimization framework, an optimum solution of the CCTM is presented in Table 2 with a reliability index value of $\beta = 3.0281$, equivalent to 99.88% reliability. With the definition of the T_e value as the position with the largest torque in the initial rotation angle set to 20^o, the preliminary expected torque is $T_e = 80.68$ *Nmm* (this is the single T_e value for one branch of the mechanism). This mechanism exhibits a large torque stability range of 88^0 with the torque values of 79.11 *Nmm* at 17^o and 82.95 *Nmm* at 105^o, respectively. Within this range, the maximum and minimum torques are 82.95 *Nmm* at 105^o and 78.48 *Nmm* at 79^o, with the corresponding deviation of 2.8% and 2.7% from the targeted torque, respectively. Therefore, the mechanism meets the requirement of output torque deviation not exceeding 3%.

The maximum stress value of the mechanism calculated from CBCM is 141.1*MPa* at the rotation angle of 105^o. The yield strength of PEEK is 210*MPa*, with a safety factor of $SF = 1.2$, resulting in an allowable stress of 175*MPa*. Hence, the maximum stress of the CCTM remains within the allowable stress limits of the material, ensuring that the mechanism operates within the elastic deformation zone. Fig. 11 illustrates the relationship between torque, stress and input rotation angle. The optimal shape of the compliant beams for a

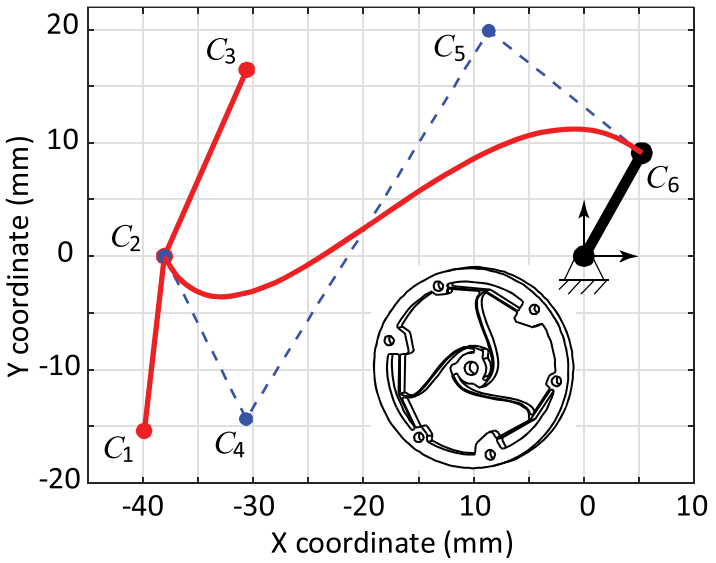

Fig. 12. Optimal beams' shape and the 3D model.

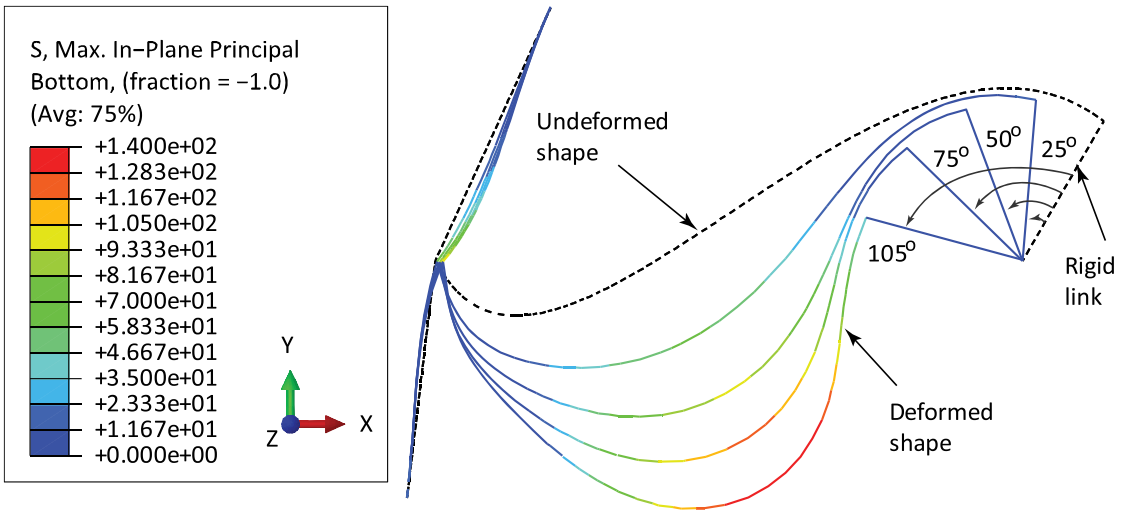

Fig. 13. FEM simulated deformed shape of the CCTM.

branch and its completed 3D configuration is also shown in Fig. 12.

3.2. FEM verification and experiments

Nonlinear FEM simulations were conducted using the commercial software ABAQUS, alongside experimental testing, to verify the results of the analytical model described previously. The curved beam was discretized into forty elements, with each straight beam divided into thirty B21 2-node linear beam elements. Similarly, the rigid link was also modeled as a 2-node element, with the geometric nonlinearity option is enable.

The torque-rotation results obtained from the FEM simulation demonstrated excellent agreement with the results from CBCM calculation, as shown in Fig. 11. The principal stress, as calculated using CBCM, was compared to the distribution of principal stress along the compliant beams using FEM simulation (Fig. 13). The maximum stress in the FEM simulation occurred at the rotation of 105^o is $140.0MPa$, which is slightly lower than the stress value predicted by CBCM ($\sigma_{max} = 141.1MPa$).

For experimental evaluation, a CCTM made from PEEK was fabricated by CNC milling. Prior to the experiment, the mechanism was tested for machining accuracy to ensure that the machining error met the STD required for the reliability analysis. A 3D scan of the actual mechanism was performed to compare it with the design model. The scanning process was conducted using an ATOS Core 300 scanner (GOM, Germany), as shown in Fig. 14(a). The actual machining profile and the design profile are presented in Fig. 14(b). This

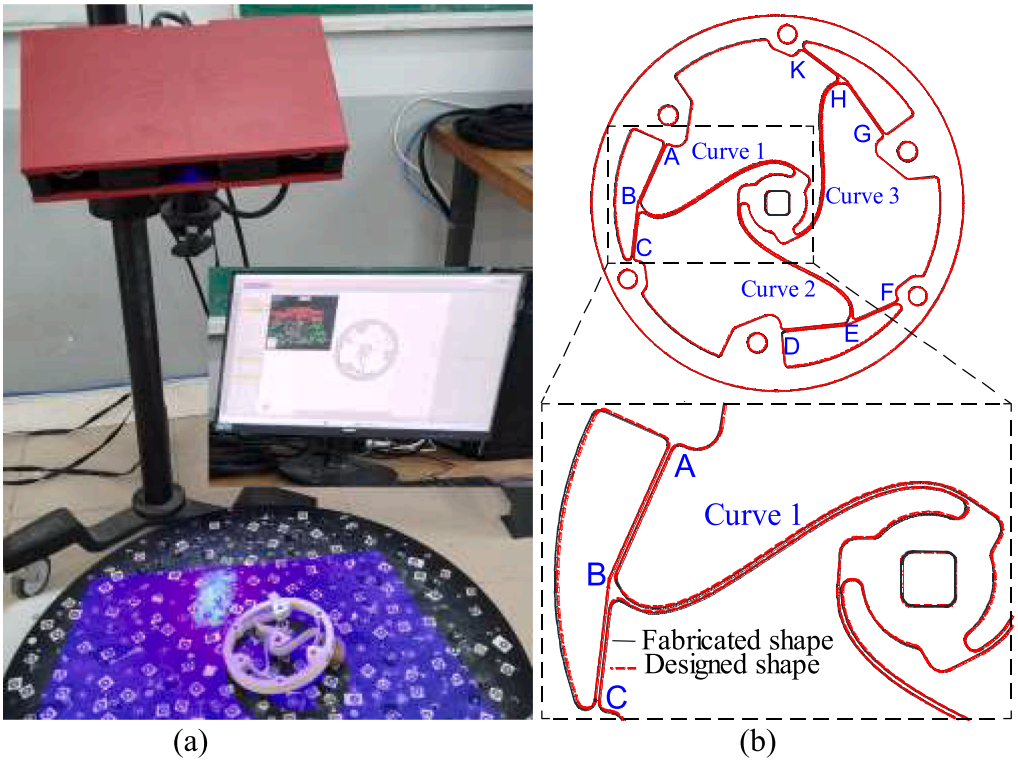

Fig. 14. (a) 3D scanning of the mechanism and (b) comparison of the 2D profiles of the actual mechanism and the designed mechanism.

Table 3
Evaluate the widths of the beams.

	Branch 1			Branch 2			Branch 3		
	Curve 1	AB	BC	Curve 2	DE	EF	Curve 3	GH	HK
Mean	0.572	0.506	0.495	0.568	0.494	0.485	0.578	0.504	0.495
STD	0.025	0.007	0.004	0.033	0.009	0.004	0.017	0.009	0.004
CoV	4.511	1.510	0.837	5.997	0.820	2.099	3.099	1.816	0.843

Table 4
Evaluate the position deviation of the actual curves.

	Curve 1	Curve 2	Curve 3
Mean	0.133	0.046	0.101
STD	0.038	0.043	0.048
CoV	28.589	94.206	48.059

comparison was carried out to evaluate the width of the beams and the shape of the curved beams.

First, the dimensions are evaluated based on the widths measured at 10 points along each straight beam and 20 points along each curved beam. Next, the mean values, STDs, and coefficients of variation of the dimensions are calculated, as shown in Table 3. With the optimal widths set at 0.53 mm for the straight beams and 0.60 mm for the curved beams, and the calculated STD of 0.05 mm, the average width values meet the required specifications. Notably, the width values of the curved beams exhibit a significantly larger STD compared to those of the straight beams. Additionally, the widths of the curved beams show greater variation, particularly at their starting positions. This indicates that achieving uniform widths along the entire length of straight beams is easier than for curved beams.

As mentioned above, the straight beams primarily serve to reduce stress and do not significantly impact the structural characteristics. Therefore, the coordinates defining their shape and position are not considered random variables for reliability evaluation. Instead, we focus on assessing the shape deviation of the curved beams by evaluating their positional deviations relative to the design. The actual and designed curved beams are represented as curves positioned within their width w. The distance between corresponding points on the actual and designed curves is measured at 20 positions. These deviation values are used to calculate the mean deviation,

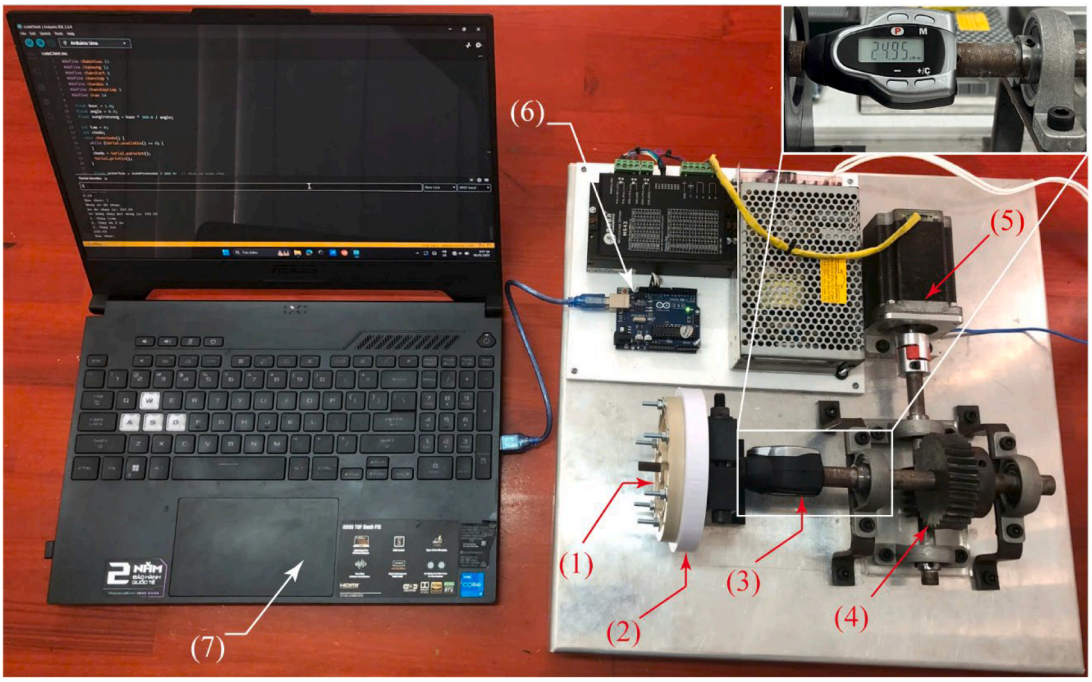

Fig. 15. Experimental setup for measuring the torque-rotation relationship.

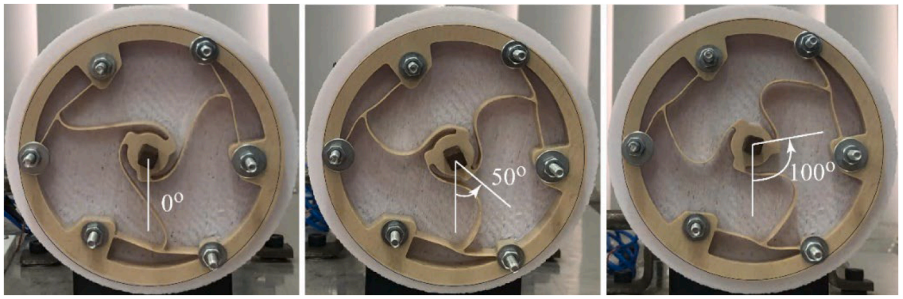

Fig. 16. Images of the CCTM in its original position and deformed at 50° and 100°.

STD, and coefficient of variation (CoV), as presented in Table 4. The results indicate that the curve 1 has the largest positional deviation from the design. However, its STD and CoV suggest that the deviation is relatively uniform. The curve 2 exhibits the highest positional agreement with the design, but its CoV value reveals significant variation in the distances between the actual and design curves. The position of the curve 2 deviates considerably at the beginning near the shaft but then closely aligns with the design curve. Overall, the STD of the positional deviations for all three curves remains within the allowable limit of 0.05.

The fabricated prototype was finally assembled into an experimental setup, as illustrated in Fig. 15. The CCTM (1) was mechanically constrained with five degrees of freedom using a planar surface and a central cylindrical guide, allowing rotation exclusively about its central axis. The outer ring of the mechanism was fixed to a mounting plate (2), which was in turn secured to a vertical support frame. To induce rotational motion, the system employed a worm drive mechanism rather than a direct-drive actuation. This configuration enabled perpendicular motion from a stepper motor (5) to be transmitted to the CCTM with high precision. The motor, controlled via an Arduino board (6) interfaced with a computer (7), drove a worm screw directly connected to its shaft, which in turn actuated a worm gear (4). This drive system rotated a digital torque screwdriver (3), which was mechanically coupled to the CCTM to produce controlled deflection.

Reaction torque was measured directly via the digital screwdriver, as indicated in the enlarged view in Fig. 15. Torque readings were recorded using a GLK060 digital torque screwdriver (KTC, Japan) at 5° rotational increments. The measurement process was repeated five times to compute average values and assess measurement uncertainty. Furthermore, the torque at a 17° position was specifically recorded for comparison with the theoretically predicted constant-torque region. The actual deformation of the mechanism in the as-fabricated configuration, as well as at various intermediate deflection states, is presented in Fig. 16.

The comparison of torque values from the analytical model, FEM simulation, and experimental results is presented in Fig. 17. To

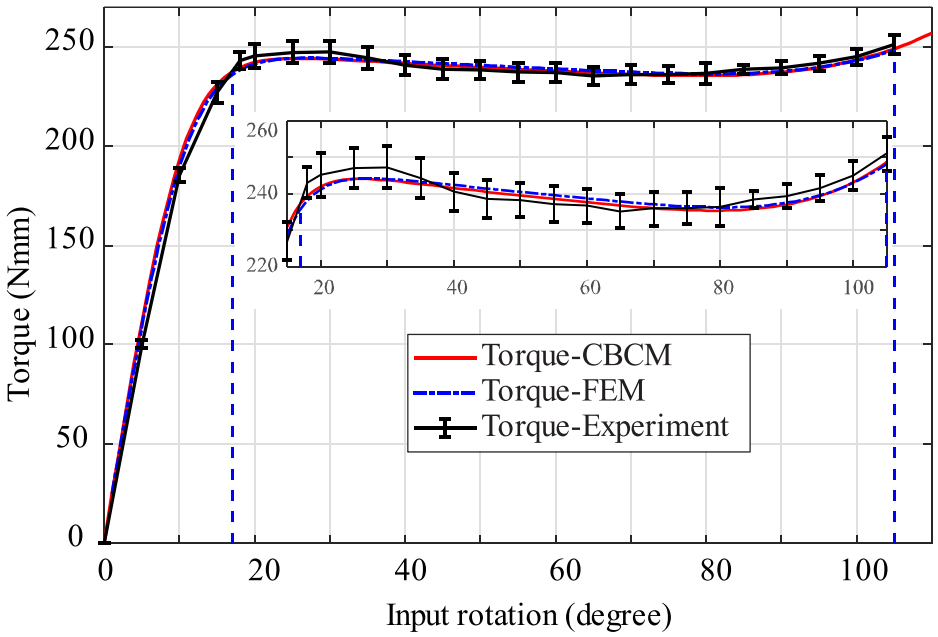

Fig. 17. Comparison of moments between CBCM, FEM and experiment.

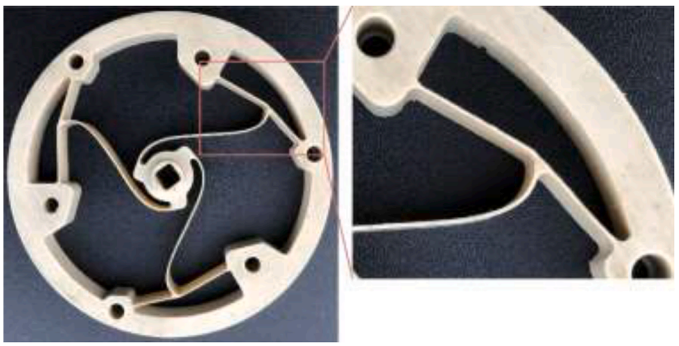

Fig. 18. Fillet at the actual intersection of three beams.

facilitate comparison, the calculated torque values from both CBCM and FEM were scaled by a factor of three to match the values measured on the actual structure. A strong agreement was observed between the CBCM and FEM results. The experimental data also closely aligned with the theoretical and simulated values. The deviation between the measured and FEM simulation values was more significant at lower rotation angles, but gradually decreased and became negligible at higher angles. The maximum deviation occurs at a rotation angle of 20^o, with an error of 1.67%. The average operational torque ranged between 17^o and 105^o was 240.4*Nmm*. The largest error of 2.9% compared to this nominal targeted torque, occurred at the 30^o rotation angle, where the torque value was 247.39*Nmm*. With an error of less than 3%, the experimental results remain within acceptable limits and meet the specified requirements.

While the mechanism meets the objectives with high reliability, the intersection of the three beams at point C_2, which was designed to reduce stress, results in greater machining errors than designs without such intersections. These errors arise because the intersection is treated as a single point in theoretical calculations using CBCM and FEM with 1-D elements, while a fillet must be introduced at this intersection in practical machining using the milling method. If the fillet is too small, the cutting tool may not be able to meet the required cutter diameter and cutting length to penetrate the full thickness of the structure.

Currently, the actual structure is being machined with a fillet radius of 1.0 mm, making the size of point C_2 larger than the simulated value, as shown in Fig. 18. In addition, variations in the measurement process and inconsistencies in the beam width, particularly in designs with intersecting beams like the current configuration of the CCTM, may contribute to errors in the experimental results. The reliability analysis above assumes uniformity in beam width along the length of the beam with random variation considered within a specific standard deviation. Further investigation in these issues will be conducted in future studies.

To evaluate the compactness of the mechanism, the non-dimensional ratio S^* of the constant-torque working range S relative to the

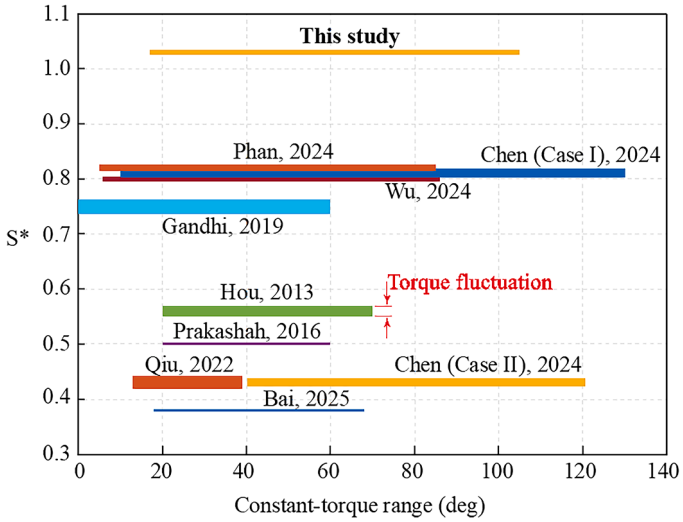

Fig. 19. Compare the proposed CCTM with published CCTMs.

overall size of the mechanism was calculated using Eq. (48). With an outer ring diameter of $D_o = 85.51\ mm$, passing through the control point C_1 (Fig. 3), the proposed CCTM exhibits the largest S^* among previously reported designs, as shown in Fig. 19. Furthermore, the fluctuation in output torque within the constant-torque range was quantified using Eq. (49) and is also illustrated in Fig. 19. The results demonstrate that the proposed CCTM achieves not only a wide constant-torque range within a compact form factor but also good torque stability compared to existing CCTMs. These findings confirm the successful design of a compact CCTM with an extended operational range, taking into account potential machining errors.

$$S^* = \frac{S}{D_o} \tag{48}$$

$$Fluctuation = 1 - \frac{T_{min}}{T_{max}} \tag{49}$$

where $\boldsymbol{T_{min}}$ and $\boldsymbol{T_{max}}$ denote the minimum and maximum torque within the constant-torque range, respectively.

In evaluating CCTMs, it is instructive to compare them with another class of statically balanced mechanisms (SBMs) exhibiting similar operational behavior, the zero-torque compliant mechanisms (CMs) [10,12,13]. While both share the fundamental goal of minimizing resistance over a defined motion range, their mechanical characteristics and application potential differ markedly. A notable example is the type-1 mechanism in Ref. [12], whose symmetric design enables bidirectional rotation, thereby increasing the rotation angle up to 80.2^o while maintaining a compact configuration ($S^* = 0.80$). However, these designs cannot sustain radial loads, limiting their use in load-bearing or force-delivery applications. While their energy efficiency and smooth motion are advantageous for certain precision positioning tasks, their functional scope differs substantially from CCTMs. Since the focus here is on CCTMs, the detailed and expanded investigation of zero-torque CMs will not be further elaborated in this paper.

Consequently, this paper has successfully presented a novel CCTM design optimized via RBDO to address fabrication uncertainties. Potential applications for this configuration include assistive devices, grippers, medical tools, or vibration isolators, as mentioned in the introduction. Real-world integration requires meeting three key criteria: large stable-torque stroke, compact size, and high output. It is an ongoing challenge and focus for future CCTM development.

4. Conclusions

This study successfully demonstrates an integrated RBDO framework for the robust design of large-stroke CCTMs, explicitly accounting for fabrication uncertainties. By combining CBCM-based modeling, FORM reliability assessment, and NSGA-II optimization, the proposed method achieves an optimum CCTM exhibiting high reliability (99.88%) and performance, with a large constant torque range of 88^o and minimal torque deviation. Theoretical analyses, FEM simulations, and experimental validation collectively confirm the efficiency of the design methodology. Furthermore, the compactness and high reliability of the optimized CCTM underscore its potential for precision applications in medical devices, robotics, and aerospace systems. This research lays the groundwork for more reliable and practical deployment of compliant mechanisms by addressing fabrication uncertainties systematically. Future studies will explore advanced manufacturing techniques and extend the methodology to multi-functional compliant mechanisms.

Declaration of generative AI and AI-assisted technologies in the writing process

During the preparation of this work the author(s) used ChatGPT-4o in order to improve the writing and enhance its fluency in English. After using this tool, the author(s) reviewed and edited the content as needed and take(s) full responsibility for the content of the publication.

CRediT authorship contribution statement

Thanh-Vu Phan: Writing – original draft, Validation, Formal analysis, Conceptualization. **Van Men Truong:** Validation, Methodology. **Huy-Tuan Pham:** Writing – review & editing, Supervision, Project administration, Methodology, Conceptualization. **Van-Khien Nguyen:** Resources, Methodology. **Amina Bukayeva:** Writing – review & editing.

Declaration of competing interest

The authors declare that they have no known competing financial interests or personal relationships that could have appeared to influence the work reported in this paper.

Acknowledgement

This work belongs to the project grant No: T2024-03 funded by Ho Chi Minh City University of Technology and Education, Vietnam.

Data availability

No data was used for the research described in the article.

References

[1] T. Liu, G. Hao, J. Zhu, P. Kuresangsai, S. Abdelaziz, E. Wehrle, Modeling compliant bistable mechanisms: an energy method based on the high-order smooth curvature model, Int. J. Mech. Sci. 275 (2024) 109315, https://doi.org/10.1016/j.ijmecsci.2024.109315. /08/01/2024.
[2] H.T. Pham, D.A. Wang, A quadristable compliant mechanism with a bistable structure embedded in a surrounding beam structure, Sens. Actuators A Phys. 167 (2) (2011) 438–448, https://doi.org/10.1016/j.sna.2011.02.044, 2011/06/01/.
[3] P. Wang, Q. Xu, Review-design and modeling of constant-force mechanisms: a survey, Mech. Mach. Theory 119 (2018) 21, https://doi.org/10.1016/j.mechmachtheory.2017.08.017.
[4] J. Ling, T. Ye, Z. Feng, Y. Zhu, Y. Li, X. Xiao, A survey on synthesis of compliant constant force/torque mechanisms, Mech. Mach. Theory 176 (2022) 104970, https://doi.org/10.1016/j.mechmachtheory.2022.104970, 2022/10/01/.
[5] H.T. Pham, D.A. Wang, A constant-force bistable mechanism for force regulation and overload protection, Mech. Mach. Theory 46 (7) (2011) 899–909, https://doi.org/10.1016/j.mechmachtheory.2011.02.008, 2011/07/01/.
[6] T.V. Phan, H.T. Pham, C.N. Truong, Design and analysis of a compliant constant-torque mechanism for rehabilitation devices, in: I.A. Parinov, S.H. Chang, B. T. Long (Eds.), Advanced Materials, Springer International Publishing, Cham, 2020, pp. 541–549.
[7] H.T. Pham, V.K. Nguyen, V.T. Mai, Shape optimization and fabrication of a parametric curved-segment prosthetic foot for amputee, J. Sci. Technol. Tech. Univ. 102 (2014) 89–95.
[8] C. Lan, J. Wang, Design of adjustable constant-force forceps for robot-assisted surgical manipulation, in: Proceedings of the IEEE International Conference on Robotics and Automation, 2011, pp. 386–391, https://doi.org/10.1109/ICRA.2011.5979556, 9-13 May 2011.
[9] Z. Cheng, T.R. Savarimuthu, S. Foong, U.X. Tan, Design of adjustable constant force/torque mechanisms for medical applications, J. Mech. Robot. (2022) 1–18, https://doi.org/10.1115/1.4054638.
[10] C. Zhang, J. He, G. Zhou, K. Wang, D. Xu, J. Zhou, Compliant quasi-zero-stiffness isolator for low-frequency torsional vibration isolation, Mech. Mach. Theory 181 (2023) 105213, https://doi.org/10.1016/j.mechmachtheory.2022.105213, 2023/03/01/.
[11] P. Wang, S. Yang, Q. Xu, Design and optimization of a new compliant rotary positioning stage with constant output torque, Int. J. Precis. Eng. Manuf. 19 (12) (2018) 1843–1850, https://doi.org/10.1007/s2541-018-0213-x.
[12] P. Bilancia, S.P. Smith, G. Berselli, S.P. Magleby, L.L. Howell, Zero torque compliant mechanisms employing pre-buckled beams, J. Mech. Des. 142 (11) (2020), https://doi.org/10.1115/1.4046810.
[13] T. Liu, S. Bi, Y. Yao, Z. Dong, Q. Yang, L. Liu, Research on zero-stiffness flexure hinge (ZSFH) based on spring four-bar linkage(4BSL), Mech. Mach. Theory 143 (2020) 103633, https://doi.org/10.1016/j.mechmachtheory.2019.103633, 2020/01/01/.
[14] T.V. Phan, H.T. Pham, Design and optimization of a large-stroke compliant constant-torque mechanism, J. Tech. Educ. Sci. 68 (2022) 93–100.
[15] L. Qiu, C. Li, S. Dai, Y. Yu, Research on the line-arc-line constant-torque flexure hinge (LAL-CTFH) based on improved pseudo-rigid-body model (PRBM), Mech. Mach. Theory 174 (2022) 104878, https://doi.org/10.1016/j.mechmachtheory.2022.104878, 2022/08/01/.
[16] H. Nair Prakashah, H. Zhou, Synthesis of constant torque compliant mechanisms, J. Mech. Robot. 8 (6) (2016), https://doi.org/10.1115/1.4034885.
[17] R. Bai, et al., Achieving high-quality and large-stroke constant torque by axial force release, Mech. Mach. Theory 205 (2025) 105869, https://doi.org/10.1016/j.mechmachtheory.2024.105869, 2025/03/01/.
[18] T.V. Phan, V.M. Truong, H.T. Pham, V.K. Nguyen, Design of a novel large-stroke compliant constant-torque mechanism based on chained beam-constraint model, J. Mech. Robot. 16 (8) (2023), https://doi.org/10.1115/1.4063980.
[19] R. Chen, et al., Design, modeling and analysis of large-stroke compliant constant torque mechanisms, Mech. Mach. Theory 202 (2024) 105760, https://doi.org/10.1016/j.mechmachtheory.2024.105760, 2024/11/01/.
[20] M. Thanaki and H. Zhou, "Synthesizing bidirectional constant torque compliant mechanisms using precompressed beams," 2018. [Online]. Available: 10.1115/IMECE2018-86469.
[21] I. Gandhi, H. Zhou, Synthesizing constant torque compliant mechanisms using precompressed beams, J. Mech. Des. 141 (1) (2018), https://doi.org/10.1115/1.4041330.
[22] M. Ling, L.L. Howell, J. Cao, G. Chen, Kinetostatic and dynamic modeling of flexure-based compliant mechanisms: a survey, Appl. Mech. Rev. 72 (3) (2020), https://doi.org/10.1115/1.4045679.

[23] F. Ma, G. Chen, Modeling large planar deflections of flexible beams in compliant mechanisms using chained beam-constraint-model, J. Mech. Robot. 8 (2) (2015), https://doi.org/10.1115/1.4031028.
[24] Q. Zhang, P. Yan, H. Wang, A curved-beam based quasi-constant force mechanism supporting large range and force-sensitive robotic manipulation, Mech. Mach. Theory 172 (2022) 104799, https://doi.org/10.1016/j.mechmachtheory.2022.104799, 2022/06/01/.
[25] G. Chen, Modeling large deflections of initially curved beams in compliant mechanisms using chained beam constraint model, J. Mech. Robot. 11 (2019) 10, https://doi.org/10.1115/1.4041585.
[26] F. Ma, G. Chen, H. Wang, Large-stroke constant-force mechanisms utilizing second buckling mode of flexible beams: evaluation metrics and design approach, J. Mech. Des. 142 (10) (2020), https://doi.org/10.1115/1.4046242.
[27] K. Wu, Q. Sun, L. Liu, Y. Liu, G. Zheng, R. Chen, Design and optimization of compliant constant-torque mechanisms utilizing arbitrary pre-curved beams, Mech. Mach. Theory 203 (2024) 105803, https://doi.org/10.1016/j.mechmachtheory.2024.105803, 2024/11/15/.
[28] C.W. Hou, C.C. Lan, Functional joint mechanisms with constant-torque outputs, Mech. Mach. Theory 62 (2013) 166–181, https://doi.org/10.1016/j.mechmachtheory.2012.12.002.
[29] S.K. Choi, R.A. Canfield, R.V. Grandhi, Reliability-Based Structural Design, Springer, 2007.
[30] A.S. Nowak, K.R. Collins, Reliability of Structures, Mc Graw-Hill, 2000.
[31] J. Tu, K.K. Choi, Y.H. Park, A new study on reliability-based design optimization, J. Mech. Des. 121 (4) (1999) 557–564, https://doi.org/10.1115/1.2829499.
[32] X. Du, W. Chen, Sequential optimization and reliability assessment method for efficient probabilistic design, J. Mech. Des. 126 (2) (2004) 225–233, https://doi.org/10.1115/1.1649968.
[33] F. Li, T. Wu, A. Badiru, M. Hu, S. Soni, A single-loop deterministic method for reliability-based design optimization, Eng. Optim. 45 (4) (2013) 435–458, https://doi.org/10.1080/0305215X.2012.685071, 2013/04/01.
[34] J. Qiu, J. Lang, A. Slocum, A curved-beam bistable mechanism, J. Microelectromech. Syst. 13 (2004) 137–146, https://doi.org/10.1109/JMEMS.2004.825308, 05/01.
[35] S. Awtar, K. Shimotsu, S. Sen, Elastic averaging in flexure mechanisms: a three-beam parallelogram flexure case study, J. Mech. Robot. 2 (4) (2010), https://doi.org/10.1115/1.4002204.
[36] K. Deb, A. Pratap, S. Agarwal, T. Meyarivan, A fast and elitist multiobjective genetic algorithm: NSGA-II, IEEE Trans. Evol. Comput. 6 (2) (2002) 182–197, https://doi.org/10.1109/4235.996017.

ASME Journal of Mechanics and Robotics
Online journal at:
https://asmedigitalcollection.asme.org/mechanismsrobotics

Thanh-Vu Phan
Faculty of Mechanical Engineering,
Ho Chi Minh City University of Technology and Education,
01 Vo Van Ngan Street,
Thu Duc City, Ho Chi Minh City 700000, Vietnam
e-mail: vupt@hcmute.edu.vn

Van Men Truong
School of Engineering and Technology,
Tra Vinh University,
126 Nguyen Thien Thanh Street, Ward 5,
Tra Vinh 87000, Vietnam
e-mail: tvmen@tvu.edu.vn

Huy-Tuan Pham[1]
Faculty of Mechanical Engineering,
Ho Chi Minh City University of Technology and Education,
01 Vo Van Ngan Street,
Thu Duc City, Ho Chi Minh City 700000, Vietnam
e-mail: phtuan@hcmute.edu.vn

Van-Khien Nguyen
Faculty of Mechanical Engineering,
Ho Chi Minh City University of Industry and Trade,
140 Le Trong Tan, Tay Thanh, Tan Phu,
Ho Chi Minh City 700000, Vietnam
e-mail: khiennv@hufi.edu.vn

Design of a Novel Large-Stroke Compliant Constant-Torque Mechanism Based on Chained Beam-Constraint Model

This study addressed the development of a novel compliant constant-torque mechanism (CCTM) that utilizes Bezier curved beams to provide a large stroke in the constant-torque operating range. Previous CCTMs are limited by their working stroke, which reduces their applicability. The proposed mechanism is based on an analytical model using the chained beam-constraint model (CBCM), which captures the kinetostatic behavior of flexible segments. A genetic algorithm based on the CBCM was used to obtain the optimal structure, which was then verified through finite element analysis and experimental results. The results show that the proposed CCTM provides good flatness with a deviation of 3.7% and a large stroke of 80 deg in the constant-torque working range, while maintaining compactness. This novel CCTM has the potential to provide a simple and effective solution for torque regulators in various applications. [DOI: 10.1115/1.4063980]

Keywords: compliant mechanisms, mechanism design, mechanism synthesis and analysis

1 Introduction

Compliant mechanisms (CMs) take advantage of monolithic structures, making them simple, compact, and lightweight, and reducing the cost of fabrication, lubrication, and maintenance. Because of their non-assembled structure, such mechanisms can be easily scaled to small sizes [1]. In terms of the function of the mechanism, CMs have special-purpose forms of bistable mechanisms [2], multistable mechanisms [3], statically balanced mechanisms [4], compliant constant-force mechanisms (CCFMs) [5], and compliant constant-torque mechanisms (CCTMs) [6]. Over the past few decades, CCTMs have been an exciting research topic [7] because of their applications in rotational mechanisms, for which constant-force mechanisms do not work [8]. Constant-torque mechanisms can produce a nearly unchanged torque, regardless of the angular input in the operational range. Hence, it has been considered as a solution for torque regulators instead of using a sophisticated feedback system. This feature of CCTMs makes them more portable and has been exploited for rehabilitative devices or mobility-assisting devices for human joints [9] and surgical applications [10].

Constant-torque mechanisms are zero-stiffness mechanisms because their torque is stable when the displacement changes. Two commonly used methods to create a compliant constant-torque mechanism (CCTM) are a combination of negative- and positive-stiffness structures and the employment of an optimal curved beam. In the first method, negative-stiffness mechanisms, which can be bistable or pre-buckled beams, are combined with a cross-axis flexure hinge [11], spiral spring, optimized curved beam, or folded beam with positive stiffness [12,13]. Based on the kinematic limb singularity, a crank-slider linkage can generate a zero-stiffness zone by varying the spring stiffness [14]. The second approach applies optimization algorithms for curved beams to obtain the desired input rotation–reaction torque curve [15,16]. These curved beams can have uniform or non-uniform widths (in-plane thickness).

Flexible segments of a CCTM must operate within the elastic deformation range of the material. Furthermore, before reaching a stable torque value, the CCTM suffers from a pre-loading range, which usually accounts for one-third of the total input displacement. This limits the working field and hampers the potential applications of CCTMs. Some studies eliminated the pre-loading range, using pre-compressed beams; however, the working range of these CCTMs was not greater than 60 deg [12,17]. Another type of

[1]Corresponding author.

Contributed by the Mechanisms and Robotics Committee of ASME for publication in the Journal of Mechanisms and Robotics. Manuscript received August 8, 2023; final manuscript received October 25, 2023; published online December 11, 2023. Assoc. Editor: Guangbo Hao.

CCTM named bidirectional CCTM can generate the output constant torque in both clockwise and counter-clockwise directions. This type of mechanism has two layers for two operation directions, so it requires an assembly to construct the structure. With pre-compressed beams, this CCTM showed a constant torque working range of each direction from 0 deg to 70 deg; however, the prototype was not fabricated for validation [18]. With the type of stiffness combination CCFM/CCTM, another approach to extend the working range is to utilize multistage negative-stiffness mechanisms [19,20] or serially connected curved beams that deform sequentially [21]. Consequently, the operating ranges of these mechanisms could be divided into multiple stages.

Curved beams have the advantages of large deflection and more uniformly distributed stress than straight beams [22,23]; therefore, they have been widely used in CCTMs. Hence, modeling nonlinear deformations is the primary task in designing CCTMs. Various methods for implementing this task are briefly reviewed in Ref. [24], including the pseudo-rigid-body method, elliptic integral solution, circle-arc method, and Adomian decomposition method. More recently, the chained beam-constraint model (CBCM), a descendent of the BCM, which is only accurate for small deflection beams [25,26], has been developed to capture force-displacement relations of large deflection beams. The CBCM has been verified as a simple and accurate method for modeling large deflections of straight [24], circular [27], and noncircular curved [28] beams. Moreover, its computational cost is lower than that of nonlinear finite element analysis (FEA) [24,28,29], which is beneficial for its incorporation in optimization algorithms when it comes to designing CCTMs.

This study aimed to design a single-stage CCTM with a working range as extensive as possible. To achieve this goal, we combined the CBCM calculation method with the non-dominated sorting genetic algorithm II (NSGA-II) to exploit the superior characteristics of both tools. NSGA-II is a multi-objective algorithm based on nature for global optimization problems with nonlinear objective functions. It is an improvement of NSGA, while NSGA is developed based on the genetic algorithm (GA) method. NSGA differs from the GA method only in the selection step, so it inherits the advantages of the GA method. However, NSGA still has limitations, such as slow computation time and dependence on control parameters. To overcome these limitations, Deb et al. proposed the NSGA-II, which not only addresses the limitations of NSGA but also ensures diversity and maintains good individuals across generations [30]. The set of all non-dominating acceptable solutions within the feasible region is called the Pareto optimal set. A practical approach to multi-objective optimization is to search for a set of solutions that represent the best possible performance within the Pareto optimal set, known as the Pareto front (the set of the best-value solutions) [31]. The CBCM accelerates the calculation of the displacement–moment response curve, thereby allowing NSGA-II to be implemented with a large number of designs in the same generation and allowing the algorithm to evolve over many generations without consuming too much time. The result obtained in this study was a CCTM with an operating range of approximately 80 deg. To the best of our knowledge, this is the largest constant-torque operating range reported to date. This extensive working range and single-stage design open up opportunities for many applications in which CCTM is used as a tool for torque control during product operations.

2 Design and Optimization

2.1 Design Concept. Constant-torque mechanisms are widely used in various applications in which a stable torque is required during device operation. Figure 1(*a*) exemplifies an application scenario of a constant-torque mechanism as a mobility-assisted device for a human's knee joint. It could help individuals with mobility impairments conveniently perform daily activities such as walking, going up and down stairs, or confidently attending

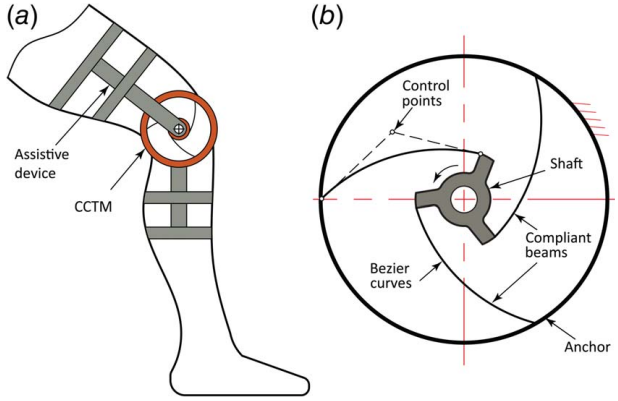

Fig. 1 (*a*) Application of a CCTM as a mobility-assisted device for human's knee joint, and (*b*) concept of large-stroke CCTM

other outdoor activities. The proposed CCTM, shown in Fig. 1(*b*), was designed based on the shape optimization method of a curved beam. The beam is parameterized using a Bezier function for convenience during the design process. A Bezier curve is a parametric curve controlled by control points. It does not go through all the control points but only through the first and last of them. This characteristic facilitates the realization of changes in the global shape without introducing too many variables. The aforementioned Bezier curved beam was polarly triplicated around a rotary shaft to ensure the symmetrical operation of the mechanism. One end of each beam was mounted on a rigid bar fixed to a shaft to receive a rotational input. The other was fixed to the outer ring, which was used as an anchor. When a particular input torque rotates the shaft, the slender curved beams are deformed. Unlike most CMs, CCTM is a special type in which the relationship between torque and rotation does not comply with Hooke's law within the elastic limit. After surpassing the pre-loading region, the mechanism reaches the working region, where the torque value remains nearly unchanged with increasing shaft rotation angle, as depicted in Fig. 2.

2.2 Curved Beam CCTMs: A Brief Overview. Before describing the design configuration used in this study to obtain a simple and large-stroke structure objective, the authors reviewed existing CCTMs based on optimal curved beams (Table 1). Hou and Lan [6] proposed two types of beams. In type I, the beam was a combination of five circular curves. Type II was a simpler form of type I when three circular arcs in the middle were replaced by a straight line to make a circular-line-circular beam. However, the stress in type II was higher than in type I because the stress

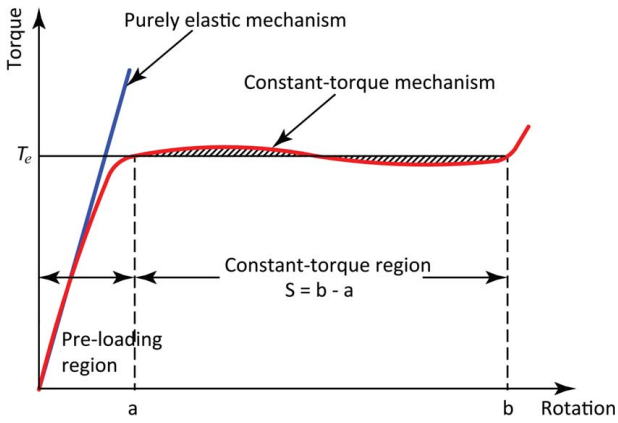

Fig. 2 Torque versus rotation angle of a CCTM

Table 1 Brief overview of CCTMs based on the optimal curved beams

Study	Characteristic of beam	Optimization method
Hou and Lan [6]	Five-circular-curve beam (Type I) Circular-line-circular beam (Type II)	Generalized multiple shooting method + *fmincon* (MATLAB)
Prakashah and Zhou [16]	Cubic variable-width spline	FEA (ANSYS) + *fmincon* (MATLAB)
Phan et al. [9]	Three-cubic-Bezier-curve beam	FEA (ABAQUS) + GA (MATLAB)
Qiu et al. [15]	Line-arc-line beam (assembly structure)	Pseudo-rigid-body model + unknown optimization algorithm
This study	Quadratic Bezier curve	Chained beam-constraint model + NSGA-II

distribution was poor in the straight shape. Phan et al. [9] combined three cubic Bezier curve segments to design devices in which two outer curves functioned as a flexible hinge to reduce the stress concentration. Prakashah and Zhou [16] used a cubic variable-width spline with five interpolation points to formulate a beam. Variable-width beams need more parameters to control their widths, so these beams were complicated compared with uniform-width beams. Qiu et al. [15] constructed a line-arc-line CCTM from simple beams; however, the entire structure of the design was complex because it was assembled from many parts. It sacrifices the advantage of CMs as monolithic structures.

2.3 Analytical Modeling. Higher-order curves may promote more novel designs but could also lead to "cusp" or "loop" phenomena in the beam shape, resulting in unfeasible mechanisms [16,32]. To avoid such phenomena, it is necessary to add more constraints, which make the optimization problem more complicated. Therefore, to simplify and avoid the above phenomena without complicating the optimization problem, a quadratic Bezier curve with three control points, $C_0(x_0,y_0)$, $C_1(x_1,y_1)$, and $C_2(x_2,y_2)$, was chosen for the slender beam in this study, as shown in Fig. 3. Given that the design is symmetrical, only one branch is illustrated and analyzed. The curved beam has a width (w) and a thickness (t) constant throughout its length. To vary its shape and achieve constant-torque mechanism characteristics, we could change eight design variables (DVs), including six coordinates of three control points as well as t and w. However, to reduce the number of DVs, point C_0, mounted on the outer ring with radius R_o, is aligned on the horizontal centerline; thus, its coordinates (x_0,y_0) are restrained to $(-R_o, 0)$. Point C_2 is attached to the inner ring with radius R_i and governed by angle γ. Radius R_i is also constrained to ensure sufficient space for assembling a shaft on it. Hence, the coordinates of point $C_2(x_2,y_2)$ become re-parameterized according to the point at the end of the Bezier curve associated with the rotational axis. Its coordinates are (R_i cos γ, R_i sin γ). The out-of-plane thickness t affects only the magnitude of the torque rather than its variation within the operational range. Thus, it was not selected as a DV. Therefore, there are only six DVs, including coordinates (x_1,y_1) of C_1, radii R_o, R_i, angle γ, and the uniform in-plane thickness w of the beam.

CBCM has been extensively studied by Chen et al., where it was successfully applied to predict force-displacement relationships for large and complex deflections of flexible beams in compliant mechanisms [24,28]. Their findings demonstrated a strong agreement between the CBCM and FEA, with the largest discrepancies in torque-input rotation relationships being only 1.75%.

In this study, we conducted a preliminary investigation to validate the accuracy of the CBCM, and the results align closely with those reported in Refs. [24,28]. Consequently, to streamline our manuscript, the authors have opted to omit the preliminary and utilized the CBCM method to obtain the angular rotation and torque relation in the optimization process. A Bezier parametric curve is typically constructed from control points C_i, where two lines of the polygon connecting the beginning and ending points of the curve coincide with the two tangent vectors of the curve at these points. To implement the CBCM calculation model for the curved beam, control point C_0 was selected as the origin of the global coordinate system XOY (Fig. 4(*a*)). To facilitate the parameterization of each point on the Bezier curve, tangent line C_0C_1 or axis OX is rotated by an angle such that it becomes horizontal in the plane (Fig. 4(*b*)).

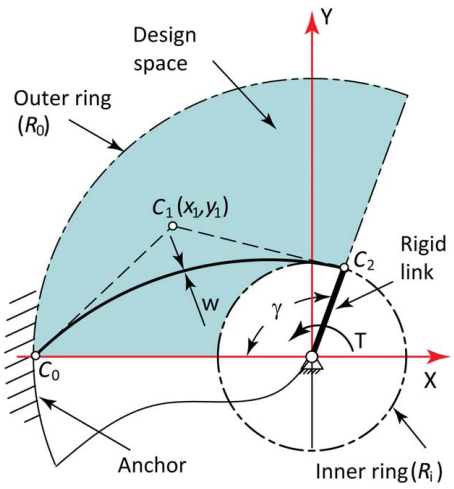

Fig. 3 DVs of the Bezier curve

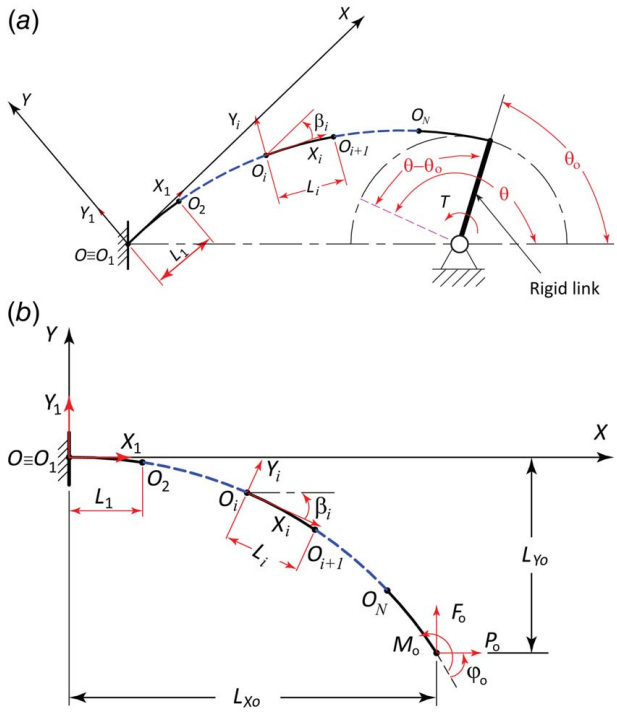

Fig. 4 Discretization of the beam at the undeflected state of the (*a*) original and (*b*) rotated positions

The free-body diagram of the curved beam in Fig. 4(*b*) illustrates that its right end is subjected to a vertical force F_o, horizontal force P_o, and moment M_o at its free end. The beam parameters include out-of-plane thickness t, in-plane thickness w, and lengths L_{X0}, L_{Y0} along the X- and Y-axes, respectively. The Young's modulus of the material is E and the moment of inertia of the beam cross section is $I = tw^3/12$.

In the CBCM approach, the beam is divided into finite elements such that each piece is applied by the BCM [33]. The more elements the beam is segmented, the more accurate the results that can be obtained; however, this also increases the computation time. A convergence study was conducted, concluding that the discretization of each beam into 20 segments was sufficient.

Each element is associated with a local coordinate system. The ith element consists of two-node O_iO_{i+1} with the coordinate system $O_iX_iY_i$ located at node i; the X_i-axis is the slope and moves along with the free end of the $(i-1)$th element. Each local coordinate creates an angle β_i with the global coordinate, where the selected $O_1X_1Y_1$ coincides with OXY or $\beta_1 = 0$. The remaining angles β_i are determined as follows:

$$\beta_i = \arccos\left(\frac{|(x_2 - x_1).(x_{i+1} - x_i) + (y_2 - y_1).(y_{i+1} - y_i)|}{\sqrt{(x_2 - x_1)^2 + (y_2 - y_1)^2}.\sqrt{(x_{i+1} - x_i)^2 + (y_{i+1} - y_i)^2}}\right), (i = 2, 3, \ldots, n+1) \tag{1}$$

The length L_i of the ith element is measured along the O_iX_i axis

$$L_i = \sqrt{(x_{i+1} - x_i)^2 + (y_{i+1} - y_i)^2} \tag{2}$$

Then we have

$$L_{X0} = \sum_{i=1}^{n} L_i \cos\beta_i \tag{3}$$

$$L_{Y0} = \sum_{i=1}^{n} L_i \sin\beta_i \tag{4}$$

The equation of a quadratic Bezier curve with three control points C_0, C_1, and C_2 is as follows:

$$P(t) = (1-t)^2 C_0 + 2t(1-t)C_1 + t^2 C_2 \tag{5}$$

where $t \in [0, 1]$. If the curve is divided into n segments, the value of t is divided in increments of $1/n$. With $n = 20$, we have 21 values of t ranging from 0 to 1 in steps of 0.05. By substituting these values of t and the coordinates of the control points into Eq. (5), we obtain the coordinates (x_i, y_i) of the points on the curve, which are used to calculate the angles and lengths using Eqs. (1) and (2).

The angle between the rigid link and OX axis in the initial and later positions (the deformed position of the CCTM) is denoted as θ_o and θ, respectively. Thus, the displacement of the mechanism is an angle ranging from 0 to $(\theta - \theta_o)$, as shown in Fig. 4(*a*).

Figure 5 depicts the ith element in the deformed and initial states. The displacement in the X and Y directions is ΔX_i and ΔY_i, respectively. The rotated angle of the ith element relative to its initial position is denoted by α_i, and the slope φ_i of the ith element after the deformation with respect to the global coordinate is defined as follows:

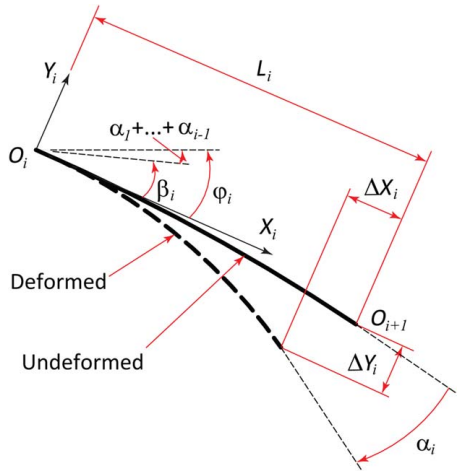

Fig. 5 The *i*th element at its deflection position

$$\varphi_i = \beta_i + \sum_{k=1}^{i-1} \alpha_k \tag{6}$$

The load–deflection relations of each element are derived using the BCM [34]:

$$\begin{bmatrix} f_i \\ m_i \end{bmatrix} = \begin{bmatrix} 12 & -6 \\ -6 & 4 \end{bmatrix}\begin{bmatrix} \delta y_i \\ \alpha_i \end{bmatrix} + p_i\begin{bmatrix} 6/5 & -1/10 \\ -1/10 & 2/15 \end{bmatrix}\begin{bmatrix} \delta y_i \\ \alpha_i \end{bmatrix} + p_i^2\begin{bmatrix} -1/700 & 1/1400 \\ 1/1400 & -11/6300 \end{bmatrix}\begin{bmatrix} \delta y_i \\ \alpha_i \end{bmatrix} \tag{7}$$

$$\delta x_i = \frac{t^2 p_i}{12L_i^2} - \frac{1}{2}\begin{bmatrix} \delta y_i & \alpha_i \end{bmatrix}\begin{bmatrix} 6/5 & -1/10 \\ -1/10 & 2/15 \end{bmatrix}\begin{bmatrix} \delta y_i \\ \alpha_i \end{bmatrix} - p_i\begin{bmatrix} \delta y_i & \alpha_i \end{bmatrix}\begin{bmatrix} -1/700 & 1/1400 \\ 1/1400 & -11/6300 \end{bmatrix}\begin{bmatrix} \delta y_i \\ \alpha_i \end{bmatrix} \tag{8}$$

where the load parameters F_i, P_i, and M_i and deflection parameters ΔX_i, ΔY_i, and α_i of the ith element are normalized as follows:

$$p_i = \frac{P_i L_i^2}{EI}; f_i = \frac{F_i L_i^2}{EI}; m_i = \frac{M_i L_i}{EI}; \delta x_i = \frac{\Delta X_i}{L_i}; \delta y_i = \frac{\Delta Y_i}{L_i}; \alpha_i = \alpha_i \tag{9}$$

The relationships between the elements are expressed by static equilibrium equations. The static equilibrium equation of the beam tip is as follows:

$$p_1 = p_o,\ f_1 = f_o,\ m_o = m_N \tag{10}$$

The static equilibrium equations between the first and the ith elements ($i = 2, 3, \ldots, n$) are as follows:

$$\begin{bmatrix} \cos\varphi_i & \sin\varphi_i & 0 \\ -\sin\varphi_i & \cos\varphi_i & 0 \\ (1+\delta x_i) & -\delta y_i & 1 \end{bmatrix}\begin{bmatrix} f_i \\ p_i \\ m_i \end{bmatrix} = \begin{bmatrix} f_1 \\ p_1 \\ m_{i-1} \end{bmatrix} \tag{11}$$

The equations governing the geometry constraints of the whole beam are defined as follows:

$$\sum_{i=1}^{n}\left[\begin{bmatrix} \cos\varphi_i & -\sin\varphi_i \\ \sin\varphi_i & \cos\varphi_i \end{bmatrix}\begin{bmatrix} L_i(1+\delta x_i) \\ L_i\delta y_i \end{bmatrix}\right] = \begin{bmatrix} LX_o - R_i\cos\beta_o + R_i\cos\beta \\ LY_o - R_i\sin\beta_o + R_i\sin\beta \end{bmatrix} \tag{12}$$

$$\sum_{i=1}^{n} \alpha_i = \theta - \theta_o \tag{13}$$

When an input rotation angle is applied, the reaction torque is expressed as follows:

$$T = F_o R_i \cos(\theta - \varphi_{20}) - P_o R_i \sin(\theta - \varphi_{20}) + M_o \tag{14}$$

The normal stress of the single element is defined as follows:

$$\sigma(x) = \sigma_b(x) + \sigma_a \tag{15}$$

where $\sigma_b(x)$ is the bending stress, and σ_a is the tensile stress due to the axial force P.

The bending stress at position x (occurring at the outermost fibers of the cross section $w/2$) is obtained once the displacement ΔY_i is achieved [24]:

$$\sigma_b(x) = \frac{M(x)}{I}\frac{w}{2} = \frac{Ew}{2L}\Delta Y'' \quad x \in [0;\ 1] \tag{16}$$

where $\Delta Y''$ is defined for two cases:

For $p > 0$, $\left(r = \sqrt{p}\right)$

$$\Delta Y'' = \frac{\tanh r \cosh(rx) - \sinh(rx)}{r} f + \frac{\cosh(rx)}{\cosh r} m \tag{17}$$

For $p < 0$, $\left(r = \sqrt{-p}\right)$

$$\Delta Y'' = \frac{\tan r \cos(rx) - \sin(rx)}{r} f + \frac{\cos(rx)}{\cos r} m \tag{18}$$

The tensile stress is calculated as follows:

$$\sigma_a = \frac{|P|}{A} = E\frac{|p|w^2}{12L^2} \tag{19}$$

2.4. Optimization. This study aimed to develop a quadratic Bezier curve–based CCTM with a stroke as large as possible and minimal deviation between the torque generated by the CCTM and the desired torque values within the limited space of R_0 and R_i. The optimal design parameters were obtained by CBCM-based NSGA-II optimization carried out in MATLAB. Two objective functions must be satisfied in the optimization problem: (1) maximize the stroke S in the constant-torque operating range, as expressed in Eq. (20); (2) minimize the deviation between the output and desired torque according to Eq. (21)

$$\text{Minimize}\left(\frac{1}{S}\right) \tag{20}$$

where $S = b - a$

$$\text{Minimize}[\text{f}\ (\theta)] = \int_a^b (T - T_e)^2 d\theta \tag{21}$$

In Eqs. (20) and (21), a and b are the boundaries of the working zone, as shown in Fig. 2. In the operating range of an ideal CCTM, the desired constant torque, T_e, is maintained regardless of the rotation angle. However, depending on the specific configuration of each design, the values of a and b are set so that the torque values $T(a)$ and $T(b)$ lie within the tolerance of ±5% of T_e. Therefore, these parameters are not predefined for the optimization process. To determine the value of T_e, a feasible condition was embedded in the optimization process. Accordingly, designs with a sinusoidal relationship between torque and rotation angle (like the graph shown in Fig. 2) are considered possible when comparing torque values. It means that the torque will initially go up, then decrease, and go up again. Then the value of T_e will be the first maximum torque point. In addition, selecting a and b must satisfy the constraint on the maximum of the constant-torque working region.

The optimization formulation is presented in Table 2. Seven constraint functions with different purposes are embedded to govern the optimization of a CCTM branch, as shown in Fig. 3. Function g_1 defines the design space to ensure the minimum length of the rigid link ($R_i \geq 10$ mm), allowing a driving shaft to fit into a center hole. It also constrains the overall dimensions of the mechanism encapsulated inside a circle of 100 mm in diameter. Point $C_1(x_1, y_1)$ is freely moved inside the annulus (R_i, R_o) and governed by the function g_2. Function g_3 seeks the initial angle (γ) of the rigid link for determining point $C_2(R_i \cos\gamma, R_i \sin\gamma)$. The bound of the uniform slender beam width is described in function g_4. Function g_5 directs the algorithm to probe the candidates with an operating range larger than 65 deg. The objective function in Eq. (21) evaluates the variation of the operating torque $T(\theta)$ to an expected torque T_e. This algorithm searches a CCTM with T_e in the range of 190–210 (Nmm) in function g_6. Finally, the function g_7 ensures that the mechanism always operates in the elastic region, where the safety factor is 1.3.

The optimization process, which was verified to be suitable for solving constrained nonlinear problems, is shown in Fig. 6; it was implemented automatically using MATLAB. The input parameters, including material properties, out-of-plane thickness, design space, and maximum rotation angle of the mechanism, are predefined. Besides, GA parameters must be defined for the operation of the algorithm, as shown in the "Define GA settings" box. First, using preliminary inputs, MATLAB randomly generates the initial population, which has $N = 40$ candidates. Each design will be regarded as feasible if it fulfills all the constraints in Table 2 before its objective functions are evaluated by the CBCM method. This first ancestor is then fed into the NSGA-II algorithm for the evolution process. The maximum number of evolved generations is $M = 100$. In each evolutionary cycle, the NSGA-II algorithm exports values of all the design parameters of the CCTM. Subsequently, these parameters are input for analytical modeling based on the CBCM method to obtain the rotation angle and torque relationship of the current CCTM. Next, the torque values concerning rotation angles from the CBCM analysis are used to evaluate the objective functions. Finally, NSGA-II calculates the fitness value of this design for comparison and further sorting with others in the current generation. Offspring is produced using a specific type of crossover and mutation. Based on nondominated sorting and crowding distance comparison, NSGA-II chooses the most appropriate individuals for the next generation and ensures the population size is still maintained at 40. The algorithm terminates when one of the two following conditions is satisfied: (1) the evolution converges or the difference between two successive generations of the objective function is less than the

Table 2 Formulation of a large-stroke CCTM optimization

(1)	Objective functions:
	• Maximize the constant-torque operating range according to Eq. (20)
	• Minimize the variation of the torque according to Eq. (21)
(2)	Design variables:
	• Control points: $C_1(x_1, y_1)$
	• In-plane thickness: w
	• Radii: R_o, R_i
	• Angle: γ
(3)	Constraints:
	(i) g_1: $10 \leq R_i < R_o \leq 50$ (mm)
	(ii) g_2: $R_i^2 \leq x_1^2 + y_1^2 \leq R_o^2$
	(iii) g_3: $\frac{\pi}{6} \leq \delta \leq \frac{2\pi}{3}$ (rad)
	(iv) g_4: $0.5 \leq w \leq 1.0$ (mm)
	(v) g_5: $b - a > 65$ (deg)
	(vi) g_6: $190 < T_e < 210$(Nmm)
	(vii) Maximum stress within the CCTM, g_7: $\sigma_m < \sigma_y$/SF

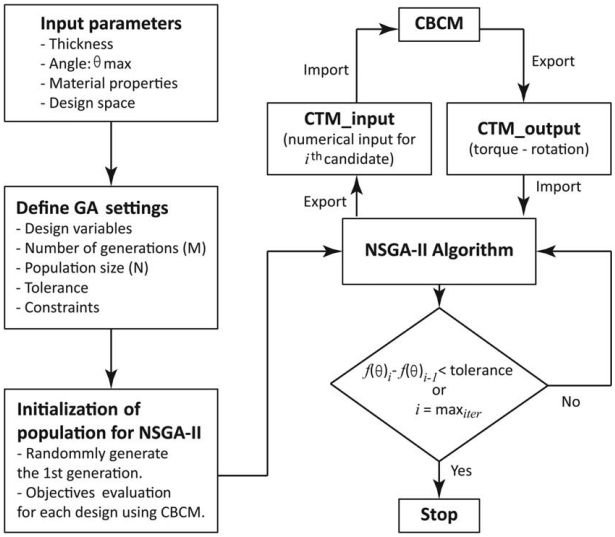

Fig. 6 Flowchart of the CBCM-based NSGA-II optimization procedure

tolerance, and (2) the initial number of generations ($\max_{iter}$) is satisfied.

It was verified that choosing an appropriate material is crucial for large-deformation mechanisms. The selected material must have a ratio σ_y/E as large as possible, representing the ability of the material to allow bending before yielding [1]. In this study, commercial polyether ether ketone (PEEK) was chosen as the structural material. For the linear elastic and isotropic model, Young's modulus (E) and Poisson's ratio (v_p) of PEEK were set as 3.58 GPa and 0.3, respectively. The out-of-plane thickness of the structure was set to 8.0 mm.

3 Results and Discussion

3.1 Optimization Results. In this study, CBCM-based NSGA-II optimization was implemented using the commercial software MATLAB. The algorithm in Fig. 6 has shown its convergence after 65 generations. The evolution of the generations is illustrated in Fig. 7. One of the optimized CCTMs in the last generation is presented in Table 3. The optimal configurations of the beam are plotted in Fig. 8(*a*), and a 3D model of the CCTM is presented in Fig. 8(*b*). The results of the optimization are shown in Fig. 9. Note that the proposed CCTM achieved an excellent flat long stroke of 80 deg ranging from 5 deg to 85 deg. The maximum stress of the mechanism was 128.16 MPa, which occurred at an input rotation angle of 85 deg. The yield strength of PEEK is 210 MPa, which ensures that the operation of the CCTM takes place in the elastic region of the material.

Table 3 Optimal design variables of the proposed CCTM

Design variables	Values	Unit
$C_1(x_1, y_1)$	(−30.9, 1.9)	mm
R_i	16.4	mm
R_o	48.8	mm
w	0.66	mm
γ	110	degree

3.2. FEA Verification and Experiments. FEA and experiments further verified the analytical modeling results. Nonlinear FEA was employed for verification using the commercial software ABAQUS. The slender beam was divided into 40 segments with a two-node linear beam element B21, whereas the rigid link was also implemented as a two-node element. The geometric nonlinearity option was switched on. The previous section used CBCM formulas to calculate bending and tensile stress developed initially from the Euler-Bernoulli beam model. However, the beam element B21 in ABAQUS is a Timoshenko beam, which further accounts for the shear deformation. This beam model only affects stubbly beams where shear effects are significant. In the case of compliant mechanisms using slender beams, the results from CBCM and FEA with Timoshenko beam elements have proven highly consistent [24,28]. In this study, the results were also similar between CBCM and FEA. As shown in Fig. 10, the maximum principal stress, occurring at node 29 of element 28, provided by FEA simulation, i.e., 123.9 MPa, was slightly lower than that of the CBCM method.

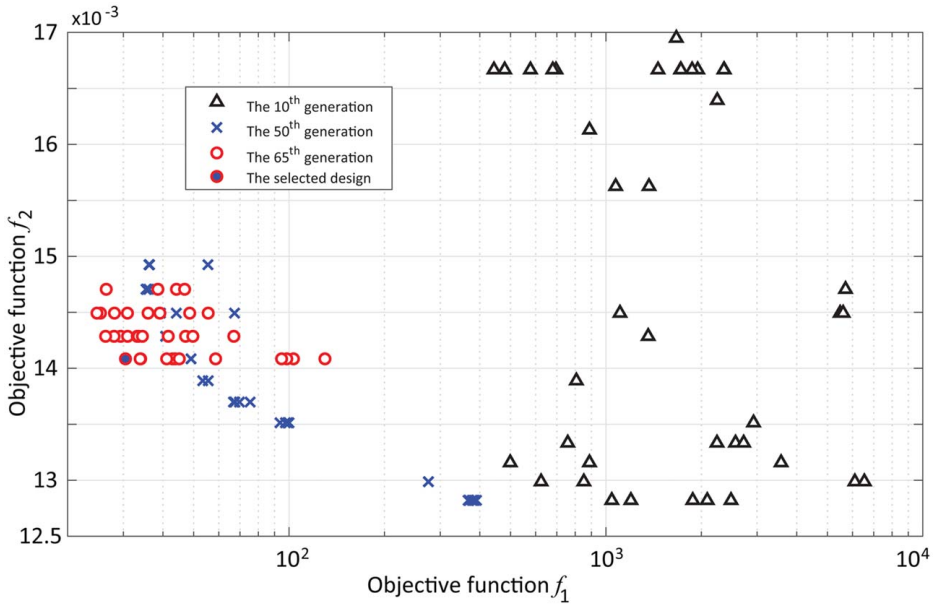

Fig. 7 Population distribution of several generations in the revolution process

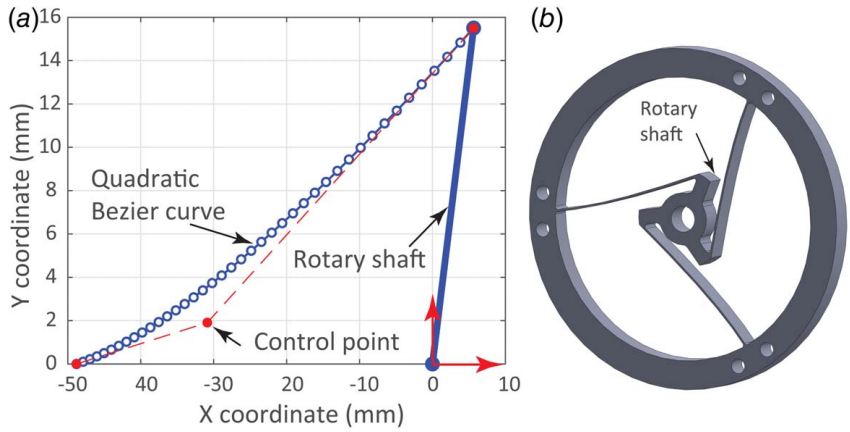

Fig. 8 (*a*) Optimal Bezier curve and (*b*) 3D model of the CCTM

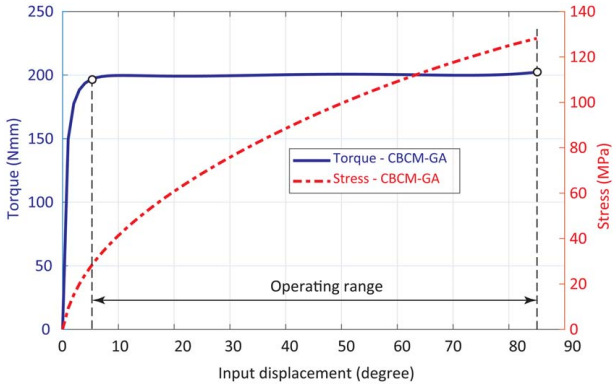

Fig. 9 Results from CBCM-based NSGA-II optimization

For experimental validation, a PEEK prototype was fabricated via a computer numerical control (CNC) milling, as shown in Fig. 11. The experimental setup is shown in Fig. 12. The outer ring of the fabricated CCTM was fixed to a plate mounted on a vertical base. The vertical base and indexing head were fixed to a vibration-isolation table using bolts to prevent ground vibration. Washers were used to avoid contact between the beams and the surface of the plate. The short cylinder ensured the concentric rotation of the three beams around the center of the mechanism. The indexing head rotated the mechanism, and the torque values were recorded at each step of 1 deg using a digital torque screwdriver from GLK060 (KTC, Japan) (Fig. 13).

The results of the analytical modeling, FEA simulation, and experiments are shown in Fig. 14. There is an excellent agreement between the CBCM and FEA results. The experimental results were higher than those of the simulation at certain points. The variation in the testing torque value compared with the average value was also greater than the predicted values, which can be explained by errors in the machining process of the flexible beams. The deviations in the output torque in the operating range are 1.5%, 0.7%, and 3.7% for the CBCM, FEA simulation, and practical model, respectively, as listed in Table 4. Since T_e was not a predefined value, the desired values were the mean values calculated from the actual minimum and maximum values. In addition, with the relatively small preload range of 5 deg, the proportion of the constant-torque operating range reached 94.1%.

Note that the larger the structure, the larger the displacement that will be achieved because a larger space between the outer and inner rings will allow compliant beams to be further deformed with a lower stress. To design a long-stroke CCTM that is still compact, the results of this study are compared in Table 5 with those of CCTMs in the literature. The non-dimensional S^* of the operational stroke with respect to the overall size (or footprint) [29,35] of the mechanism was utilized to evaluate this aspect

$$S^* = \frac{S}{D_o} \tag{22}$$

where S is the stroke, $D_o = 2R_o$, and R_o is illustrated in Fig. 3.

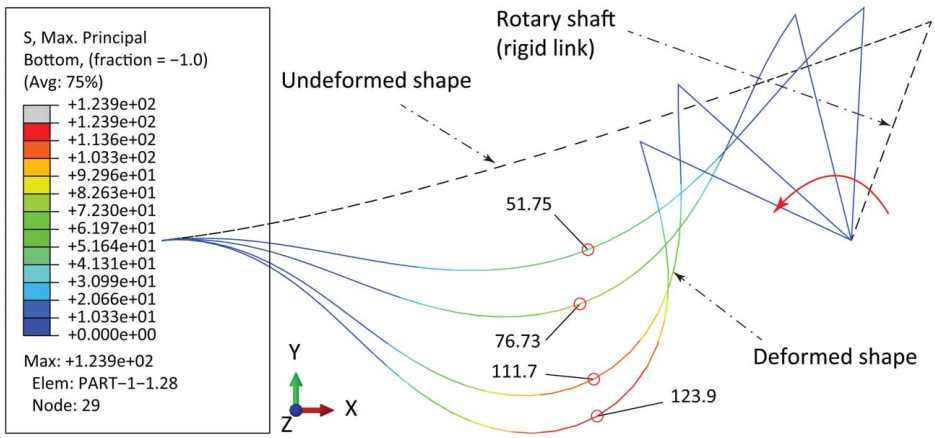

Fig. 10 Simulation results using ABAQUS

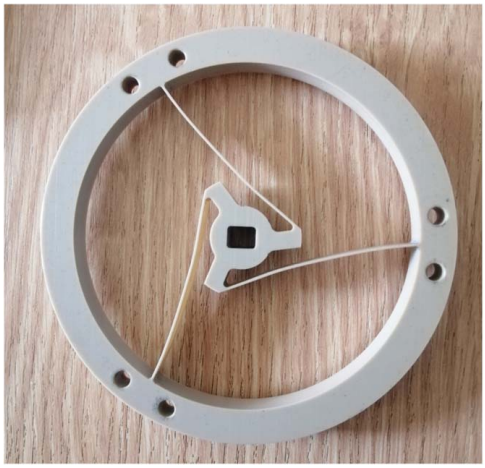

Fig. 11 Fabricated CCTM prototype

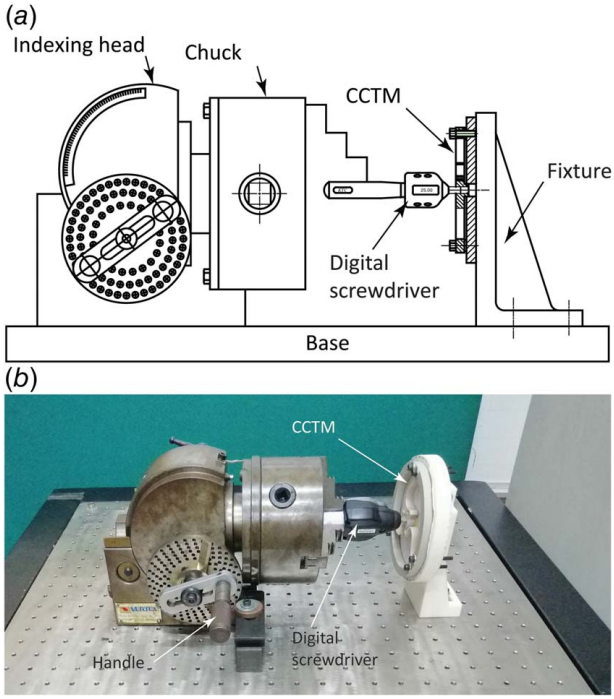

Fig. 12 Experimental setup: (*a*) design and (*b*) actual testing model

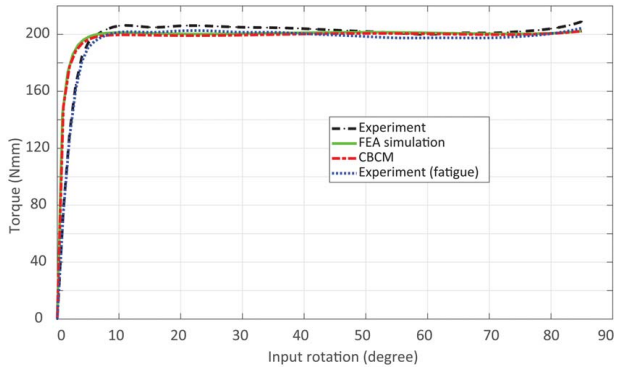

Fig. 14 Comparison of the results from CBCM, FEA, and prototype

Table 4 Output torque deviation

Model	Average value	Minimum (at 5 deg)	Maximum (at 85 deg)	Maximum deviation (%)
CBCM	199.35	196.4	202.3	1.5
FEA	198.3	196.9	199.7	0.7
Experiment	201.5	194.0	209.0	3.7

As shown in Table 5, the proposed CCTM achieves the largest S stroke and S^*. This indicates that the proposed design accomplishes the objective of realizing a larger constant-torque operating range while ensuring a compact structure.

3.3 Reliability Test. Although CMs are becoming increasingly popular in engineering design because of their advantages over traditional rigid mechanisms, they are susceptible to fatigue and failure because of the concentrated stress that can occur at critical points in the mechanism. This is particularly relevant for CMs with large strokes, which may experience high stress concentrations over a large range of motion. Therefore, fatigue testing is a critical step in the design and development of CMs.

This study conducted a reliability test on the proposed CCTM to investigate its behavior after several cycles of operation using a fatigue testing machine, as shown in Fig. 15(*b*). The device was designed to simulate the cyclic load conditions experienced by the CCTM during its intended use. The machine principle of load application is presented in Fig. 15(*a*); note that the pneumatic cylinder pushes the rack to engage with the gear to rotate the CCTM. The mechanism was not destroyed after 10,000 cycles of

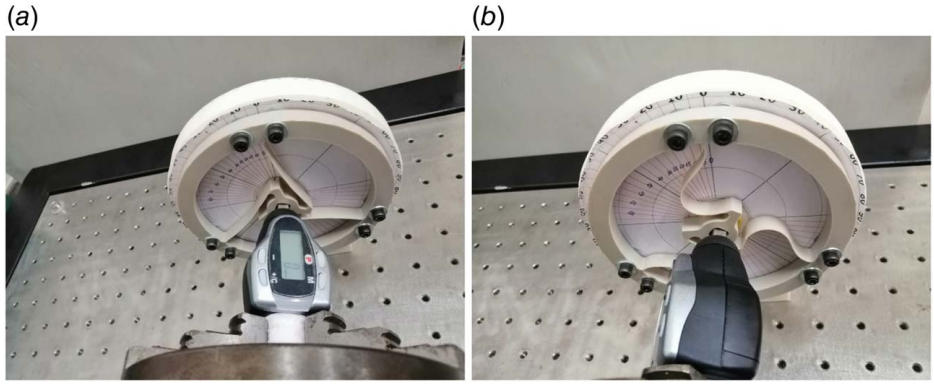

Fig. 13 Prototype at different input angles: (*a*) initial position 0 deg and (*b*) deformed shape 85 deg

Table 5 Comparison of the proposed CCTM with previous designs

Study	S (degree)	D_o (mm)	S^*
Hou and Lan [6]	50	90	0.56
Prakashah and Zhou [16]	40	80	0.50
Gandhi and Zhou [17]	60	80	0.75
Bilancia et al. [12]	40	100	0.40
Qiu et al. [15]	26	60	0.43
This study	80	97.6	0.82

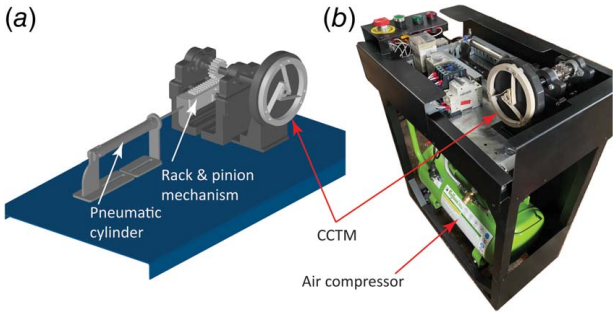

Fig. 15 Fatigue testing machine for the proposed CCTM: (*a*) CAD design and (*b*) practical testing equipment

operation. As shown in Fig. 14, the torque stability characteristic after the fatigue test was still maintained. However, the torque value was slightly reduced by about 1.7%. It should result from the material stiffness reduction after the number of fatigue cycles. These data demonstrate the reliability of the CCTM and ensure that it will perform as expected over its intended lifespan.

To increase the lifespan of a structure and prevent fatigue failure, it is necessary to add an objective function to the optimization algorithm. The objective function can be used to minimize the stress concentration in critical areas of the mechanism, thereby reducing the risk of fatigue failure. With the NSGA-II optimization algorithm, it is possible to implement this easily and efficiently, leading to more reliable and robust compliant mechanisms in the future.

4 Conclusions

This study proposes a novel single-stage large-stroke CCTM with a simple structure consisting of three quadratic Bezier curved beams. An analytical model based on the CBCM was used to establish the relationship between the output torque, stress, and input rotation. This model was optimized using NSGA-II and implemented automatically in MATLAB. The CBCM and FEA results were consistent with deviations within the desired values of 1.8% and 1.6%, respectively. The proposed CCTM was validated by fabricating a prototype using CNC machining. It exhibited a large stroke of 80 deg in the constant-torque operating range while maintaining compactness compared to other CCTMs. Furthermore, with the relatively small preload range of 5 deg, this simple structure CCTM showed a notable ratio of the constant-torque working range of 94.1%. Finally, a fatigue test was performed to verify the efficiency and applicability of the proposed method. The results demonstrate the potential of this novel CCTM as a simple and effective solution for torque regulation in various applications.

Funding Data

- Ho Chi Minh City University of Technology and Education, Vietnam (Grant No: T2022-78).

Conflict of Interest

There are no conflicts of interest.

Data Availability Statement

The datasets generated and supporting the findings of this article are obtainable from the corresponding author upon reasonable request.

Nomenclature

t = out-of-plane thickness of the curved beams
w = width (in-plane thickness) of the curved beams
E = Young's modulus of the material
I = moment of inertia of the beam cross section
S = constant-torque working stroke
T = reaction torque at the center of the CCTM
f_i = normalized state of F_i
m_i = normalized state of M_i
p_i = normalized state of P_i
C_i = control points, $i = 0, 1, 2$
F_i = radial force (or vertical force) applied to the i^{th} element
F_o = radial force (or vertical force) applied to the beam tip
L_i = length of the ith element measured along the O_iX_i axis
L_{XO} = length of the beam measured along the OX axis
L_{YO} = length of the beam measured along the OY axis
M_i = moment applied to the ith element
M_o = moment applied to the beam tip
P_i = tangential force (or horizontal force) applied to the ith element
P_o = tangential force (or horizontal force) applied to the beam tip
R_i = radius of the inner ring
R_o = radius of the outer ring
a, b = boundary of the constant-torque working range
(x_i, y_i) = coordinates of the control points ($i = 0, 1, 2$) or of the point O_i ($i = 2, 3, \ldots, n+1$) with respect to the global coordinate system XOY
γ = angle determines the control point C_2
θ = initial position of the rigid link
σ = normal stress of the single element
α_i = rotated angle of the ith element relative to its position
β_i = angle between each local coordinate of the ith element and the global coordinate
θ_o = later position of the rigid link (the deformed position of the CCTM)
σ_a = tensile stress
σ_b = bending stress
φ_i = slope of the ith element after the deformation with respect to the global coordinate
δx_i = normalized state of ΔX_i
δy_i = normalized state of ΔY_i
ΔX_i = deformation in the X direction of the ith element
ΔY_i = deformation in the Y direction of the ith element

References

[1] Howell, L. L., 2001, *Compliant Mechanisms*, Wiley, New York.
[2] Qiu, J., Lang, J., and Slocum, A., 2004, "A Curved-Beam Bistable Mechanism," J. Microelectromech. Syst., **13**(2), pp. 137–146.
[3] Pham, H.-T., and Wang, D.-A., 2011, "A Quadristable Compliant Mechanism With a Bistable Structure Embedded in a Surrounding Beam Structure," Sens. Actuators, A, **167**(2), pp. 438–448.
[4] Lamers, A. J., Gallego Sánchez, J. A., and Herder, J. L., 2015, "Design of a Statically Balanced Fully Compliant Grasper," Mech. Mach. Theory, **92**, pp. 230–239.
[5] Pham, H.-T., and Wang, D.-A., 2011, "A Constant-Force Bistable Mechanism for Force Regulation and Overload Protection," Mech. Mach. Theory, **46**(7), pp. 899–909.
[6] Hou, C.-W., and Lan, C.-C., 2013, "Functional Joint Mechanisms With Constant-Torque Outputs," Mech. Mach. Theory, **62**, pp. 166–181.

[7] Saerens, E., Furnémont, R., Legrand, J., Langlois, K., López García, P., Crispel, S., Rossini, M., Verstraten, T., Vanderborght, B., and Lefeber, D., 2022, "Constant Torque Mechanisms: A Survey," ASME Appl. Mech. Rev., **74**(1), p. 010802.
[8] Ling, J., Ye, T., Feng, Z., Zhu, Y., Li, Y., and Xiao, X., 2022, "A Survey on Synthesis of Compliant Constant Force/Torque Mechanisms," Mech. Mach. Theory, **176**, p. 104970.
[9] Phan, T.-V., Pham, H.-T., and Truong, C.-N., 2020, "Design and Analysis of a Compliant Constant-Torque Mechanism for Rehabilitation Devices," Proc. Advanced Materials, Hanoi, Vietnam, Nov. 7–10, pp. 541–549.
[10] Cheng, Z., Savarimuthu, T. R., Foong, S., and Tan, U. X., 2023, "Design of Adjustable Constant Force/Torque Mechanisms for Medical Applications," ASME J. Mech. Rob., **15**(2), p. 025001.
[11] Wang, P., Yang, S., and Xu, Q., 2018, "Design and Optimization of a New Compliant Rotary Positioning Stage With Constant Output Torque," Int. J. Precis. Eng. Manuf., **19**(12), pp. 1843–1850.
[12] Bilancia, P., Smith, S. P., Berselli, G., Magleby, S. P., and Howell, L. L., 2020, "Zero Torque Compliant Mechanisms Employing Pre-Buckled Beams," ASME J. Mech. Des., **142**(11), p. 113301.
[13] Zhang, C., He, J., Zhou, G., Wang, K., Xu, D., and Zhou, J., 2023, "Compliant Quasi-Zero-Stiffness Isolator for Low-Frequency Torsional Vibration Isolation," Mech. Mach. Theory, **181**, p. 105213.
[14] Li, B., and Hao, G., 2019, "On Generating Expected Kinetostatic Nonlinear Stiffness Characteristics by the Kinematic Limb-Singularity of a Crank-Slider Linkage With Springs," Chin. J. Mech. Eng., **32**(1), p. 54.
[15] Qiu, L., Li, C., Dai, S., and Yu, Y., 2022, "Research on the Line-Arc-Line Constant-Torque Flexure Hinge (LAL-CTFH) Based on Improved Pseudo-Rigid-Body Model (PRBM)," Mech. Mach. Theory, **174**, p. 104878.
[16] Prakashah, H. N., and Zhou, H., 2016, "Synthesis of Constant Torque Compliant Mechanisms," ASME J. Mech. Rob., **8**(6), p. 064503.
[17] Gandhi, I., and Zhou, H., 2018, "Synthesizing Constant Torque Compliant Mechanisms Using Precompressed Beams," ASME J. Mech. Des., **141**(1), p. 014501.
[18] Thanaki, M., and Zhou, H., 2018, "Synthesizing Bidirectional Constant Torque Compliant Mechanisms Using Precompressed Beams," ASME 2018 International Mechanical Engineering Congress and Exposition, Pittsburgh, PA, Nov. 9–15.
[19] Ye, T., Ling, J., Kang, X., Feng, Z., and Xiao, X., 2021, "A Novel Two-Stage Constant Force Compliant Microgripper," ASME J. Mech. Des., **143**(5), p. 053302.
[20] Xu, Q., 2017, "Design of a Large-Stroke Bistable Mechanism for the Application in Constant-Force Micropositioning Stage," ASME J. Mech. Rob., **9**(1), p. 011006.
[21] Phan, T.-V., and Pham, H.-T., 2022, "Design and Optimization of a Large-Stroke Compliant Constant-Torque Mechanism," J. Tech. Educ. Sci., **68**, pp. 93–100.
[22] Rai, A. K., Saxena, A., and Mankame, N. D., 2006, "Synthesis of Path Generating Compliant Mechanisms Using Initially Curved Frame Elements," ASME J. Mech. Des., **129**(10), pp. 1056–1063.
[23] Venkiteswaran, V. K., and Su, H.-J., 2016, "Pseudo-Rigid-Body Models for Circular Beams Under Combined Tip Loads," Mech. Mach. Theory, **106**, pp. 80–93.
[24] Ma, F., and Chen, G., 2015, "Modeling Large Planar Deflections of Flexible Beams in Compliant Mechanisms Using Chained Beam-Constraint-Model," ASME J. Mech. Rob., **8**(2), p. 021018.
[25] Awtar, S., Slocum, A. H., and Sevincer, E., 2006, "Characteristics of Beam-Based Flexure Modules," ASME J. Mech. Des., **129**(6), pp. 625–639.
[26] Shusheng, B., Hongzhe, Z., and Jingjun, Y., 2009, "Modeling of a Cartwheel Flexural Pivot," ASME J. Mech. Des., **131**(6), p. 061010.
[27] Zhang, Q., Yan, P., and Wang, H., 2022, "A Curved-Beam Based Quasi-Constant Force Mechanism Supporting Large Range and Force-Sensitive Robotic Manipulation," Mech. Mach. Theory, **172**, p. 104799.
[28] Chen, G., 2019, "Modeling Large Deflections of Initially Curved Beams in Compliant Mechanisms Using Chained Beam Constraint Model," ASME J. Mech. Rob., **11**(1), p. 011002.
[29] Ma, F., Chen, G., and Wang, H., 2020, "Large-Stroke Constant-Force Mechanisms Utilizing Second Buckling Mode of Flexible Beams: Evaluation Metrics and Design Approach," ASME J. Mech. Des., **142**(10), p. 103303.
[30] Deb, K., Pratap, A., Agarwal, S., and Meyarivan, T., 2002, "A Fast and Elitist Multiobjective Genetic Algorithm: NSGA-II," IEEE Trans. Evol. Comput., **6**(2), pp. 182–197.
[31] Deb, K., Agrawal, S., Pratap, A., and Meyarivan, T., "A Fast Elitist Non-Dominated Sorting Genetic Algorithm for Multi-Objective Optimization: NSGA-II," Proc. Parallel Problem Solving From Nature PPSN VI, Paris, France, Sept. 18–20, pp. 849–858.
[32] Zhou, H., and Ting, K.-L., 2005, "Shape and Size Synthesis of Compliant Mechanisms Using Wide Curve Theory," ASME J. Mech. Des., **128**(3), pp. 551–558.
[33] Awtar, S., and Sen, S., 2010, "A Generalized Constraint Model for Two-Dimensional Beam Flexures: Nonlinear Load-Displacement Formulation," ASME J. Mech. Des., **132**(8), p. 081008.
[34] Awtar, S., Shimotsu, K., and Sen, S., 2010, "Elastic Averaging in Flexure Mechanisms: A Three-Beam Parallelogram Flexure Case Study," ASME J. Mech. Rob., **2**(4), p. 041006.
[35] Mackay, A. B., Smith, D. G., Magleby, S. P., Jensen, B. D., and Howell, L. L., 2012, "Metrics for Evaluation and Design of Large-Displacement Linear-Motion Compliant Mechanisms," ASME J. Mech. Des., **134**(1), p. 011008.

JTE
HCMUTE
ISSN: 2615-9740

JOURNAL OF TECHNICAL EDUCATION SCIENCE
Ho Chi Minh City University of Technology and Education
Website: https://jte.hcmute.edu.vn/
Email: jte@hcmute.edu.vn

Design and Optimization of a Large-Stroke Compliant Constant-Torque Mechanism

Thanh-Vu Phan, Huy-Tuan Pham *
HCMC University of Technology and Education, Vietnam
* Corresponding author. *Email: phtuan@hcmute.edu.vn*

ARTICLE INFO

Received: 18/12/2021
Revised: 26/1/2022
Accepted: 26/1/2022
Published: 28/2/2022

KEYWORDS

Constant-torque mechanism;
Compliant mechanism;
Genetic algorithm;
Finite element analysis;
Rotary mechanism.

ABSTRACT

Compliant constant-torque mechanism (CTM) can produce an output torque that does not change within a prescribed input rotation range. This stability is maintained regardless of complicated sensorized control systems. Owing to the monolithic nature of the compliant mechanism, the device is more compact, lightweight, and portable, which is favorable to human joint rehabilitative devices or mobility-assisting devices. However, before approaching the stable range, the mechanism has to undergo a pre-loading range which usually accounts for one-third of the entire operational journey. In addition, the deformation of flexible segments is restricted due to the yield strength of the materials. This limited working range hampers other potential applications of compliant CTMs. This paper presents a novel design of a compliant 2-stage CTM with long-stroke by using serially connected curved beams that deform sequentially. The design process is implemented via a shape optimization scheme using genetic algorithm. Finite element analysis is used to characterize the constant-torque behavior of the CTM under static loading. A general design formulation is also proposed to synthesize this special kind of compliant mechanism. The results show that this CTM gets the stable torque range from 30^0 to 110^0 over two stages with the deviation less than 4.3%.

Doi: https://doi.org/10.54644/jte.68.2022.1098

1. Introduction

Unlike traditional rigid-body mechanisms, compliant mechanisms (CMs) are mechanical devices that achieve motion via elastic deformation of flexible segments. CMs take advantage of a monolithic structure including no backlash, no friction, no wear, no lubrication but still ease of fabrication [1]. Constant-torque mechanism (CTM) is a variant of constant-force mechanism (CFM) which has been attracting many researchers for decades [2-13]. CTMs generate an unchanged output torque regardless of the input rotation. Such mechanisms make the force control process become much simpler instead of using a complicated feedback system with actuators and sensors [14-17]. Hence, CTMs have plenty of potential applications in medical equipment such as mobility-assisting or rehabilitative devices, dynamic and static balancing of machines [18] as well as aerospace applications [19].

Compared to the blooming development of the counterpart CFMs during the last decades, compliant CTMs have just been noticing in recent years. Hou et al. designed a compliant CTM used as a functional joint mechanism [18]. Other compliant CTMs were synthesized by employing variable-width spline curves [20] or straight beams [21]. In our previous work [22], a novel design of a CTM for a rehabilitation device was developed by using Bezier curves. The major obstacle of all compliant CTMs during their trips to the operational range is that they have to undergo the preloading range which usually amounts to one-third of the total angular motion. In addition, the deformation of flexible members is restricted due to the yield strength of materials. This limited working range hampers other potential applications of compliant CTMs. In recent literature, this dilemma is eradicated by using pre-compressed beams as building blocks for compliant CTMs [23, 24]. Regardless of all these efforts, their absolute working ranges are still humble.

JTE
HCMUTE
ISSN: 2615-9740

JOURNAL OF TECHNICAL EDUCATION SCIENCE
Ho Chi Minh City University of Technology and Education
Website: https://jte.hcmute.edu.vn/
Email: jte@hcmute.edu.vn

The concept of creating a CTM in this paper is to regulate the torque-rotation curve of a bi-stable mechanism to convert the negative stiffness region into a zero stiffness section. In order to further prolonging the working range of the CTM, this research proposes stacking two CTMs in a serial manner whilst maintaining the overall compactness of the device.

2. Design

2.1 Design concept and Operational principle

Instead of abiding by Hooke's law like conventional CMs, CTMs exhibit an irregular torque curve that radically differs from the purely elastic mechanism as shown in Fig. 1. After the pre-stress range, the mechanism approaches the quasi-zero stiffness in the constant-torque range. The output torque is stable irrespective of the variation of the input rotation. In this research, two stages of CTMs are serially connected which will lead to the sequential operation of each stage depending on their stiffness.

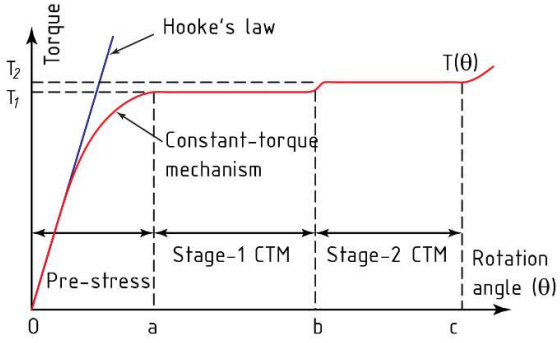

Fig. 1 - *Torque – rotation curve of a stacked compliant CTM.*

The schematic of a long-stroke CTM in this paper is proposed in Fig. 2. The idea of inducing a constant torque reaction while the CM deforms is to exploit the snap-through behavior of a specially designed curved beam as shown in Fig. 2(a). In this paper, Bezier curve is used to parameterize these beams. A reasonable circumferential arrangement of three alike beams will facilitate its axially symmetric deformation. In order to maintain the overall small size, two-stage CTMs with different stiffness are designed.

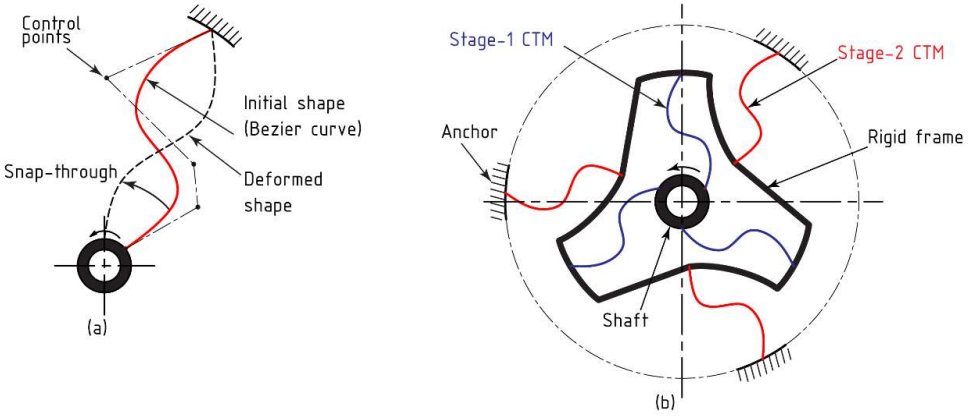

Fig. 2- *Schematic design of a CTM (a) and its 2-stages long-stroke design concept (b).*

In Fig. 2(b), three inner beams of the stage-1 CTM are mounted on a ring associated with a shaft providing the input rotation. Their other ends are linked to a rigid frame to transfer the rotational motion to three outer beams of the stage-2 CTM. These outer curved beams, which have fixed ends by the anchors, will continue deforming after receiving the motion.

JTE
HCMUTE
ISSN: 2615-9740

JOURNAL OF TECHNICAL EDUCATION SCIENCE
Ho Chi Minh City University of Technology and Education
Website: https://jte.hcmute.edu.vn/
Email: jte@hcmute.edu.vn

2.2 Optimization design of the CTM.

Shape and size of the curves are obtained via an optimization of Genetic Algorithm (GA) carried out in MATLAB, and verified by means of finite element analysis (FEA) conducted in ABAQUS. To define the shape of Bezier curves, control points must be determined. Owing to the symmetry of the design, only one branch of each level illustrated as beam 1 and beam 2 is analyzed, shown in Fig. 3.

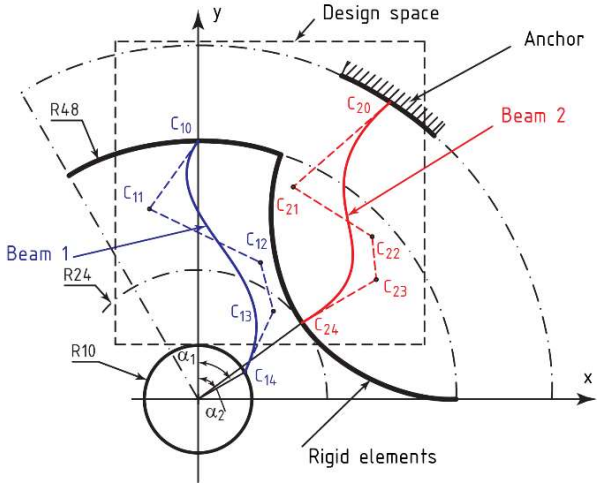

Fig. 3- *Schematic of the design variables*

For the sake of simplicity, fourth-order Bezier curve beams are chosen for the two beams. As a rule of thumb, the computer resources consumption is usually proportional to the number of design variables. Therefore some parameters of the CTM are constrained. Here, radii of the outer end of beam 1 and the inner end of beam 2 are predefined as R48 and R24, respectively. Radius of the center annular shape that attaches to point C_{14} is also a predefined parameter (R10) so that it could provide enough space to set up the shaft. The control point C_{10} is constrained to the vertical centerline and it is the intersection of this line with the circle R48. Therefore, there are totally 17 design variables including the (x, y) coordinates of C_{11}, C_{12}, C_{13}, C_{20}, C_{21}, C_{22}, C_{23} and the angles (α_1, α_2)defining C_{14}, C_{24}, respectively, as well as a uniform width (w) of the beams.

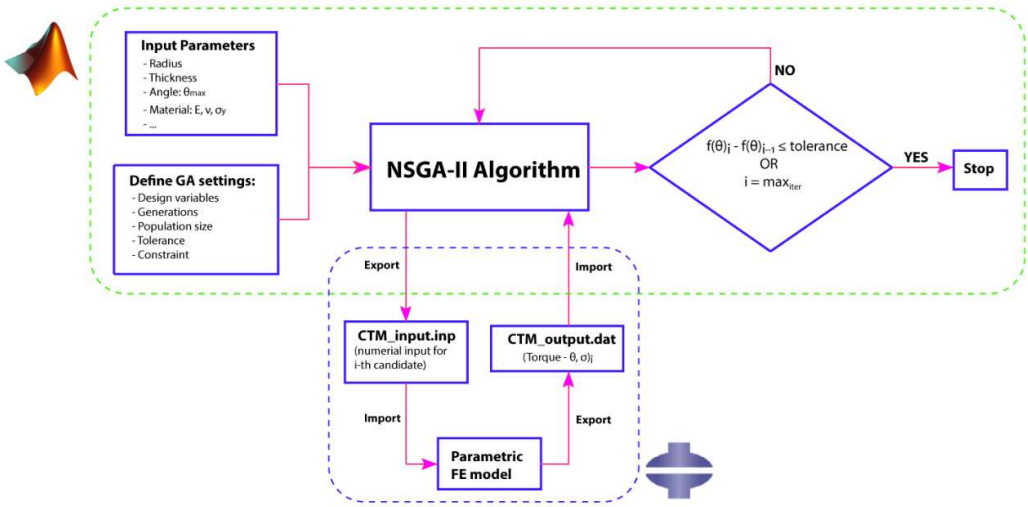

Fig. 4 - *Flowchart of the FEA-based genetic algorithm optimization procedure*

Trial designs are randomly created by using MATLAB based on the preliminary parameters. FEA by ABAQUS is applied to obtain the behavior between output torque and rotation angle. Simultaneously, the stress is also evaluated to assure the operation of the CTM within the elastic regime. To simulate precisely the relationship of flexible segments, the outer end of beam 1 (C_{10}) must rotate on the circle R48. Thus, FEA is applied for all six beams. The rigid links are replaced by 2-node beam elements for easier simulation. The flowchart of the GA which was verified to be suitable for solving constrained nonlinear problems is given in Fig. 4. The optimization was implemented automatically by MATLAB and ABAQUS. Inputs to the GA optimization are divided into two different boxes for the sake of better understanding of the algorithm. The "Input Parameters" and the "Define GA settings" boxes define the shape of the mechanism and the GA's parameters, respectively. In the first loop, MATLAB produces the text codes "CTM_iput.txt" to define the simulation model based on the design parameters generated by GA. This model is then fed into the ABAQUS to implement the analysis. The torque – rotation curve is extracted from the simulation output file to evaluate the objective function in eq. (1). It is finally returned to the GA to calculate the fitness value for further sorting this design in the current generation. The nondominated-sorting genetic algorithm (NSGA-II) generates offspring using a specific type of crossover and mutation and then selects the next generation according to nondominated-sorting and crowding distance comparison. The algorithm is terminated when the objective function difference between two successive generations is smaller than the tolerance, the evolution is converged, or the initial number of generations (max_{iter}) is met. The optimization problem in this research is formulated in the following objective function:

$$\mathrm{Min}[f(\theta)] = \int_a^b (T - T_1)^2 \, d\theta + \int_b^c (T - T_2)^2 \, d\theta \quad (1)$$

In eq. (1), a, b, and c are the margin between the pre-stress zone and the two working zones. The purpose of the objective function obtained in eq. (1) is to minimize the variation of the torque function $T(\theta)$ toward the two constant torques (T_1 and T_2) regardless the rotation angle of the mechanism in the working range. The numerical integration limits (a, b) and (b, c) depend on the configuration of the practical torque curve for each design. The criteria to choose these points is that $T(a), T(b), and\ T(c)$ should be within the tolerance of $\pm 5\%$ of T_1 and T_2. Therefore, they are not predefined parameters of the optimization process. Generally, the optimization formulation is described in Table 1. To constraint the design space as well as to reduce the number of design variables, three radii are appropriately chosen for the purpose of CTM and prescribed as 10 mm, 24 mm, 48 mm, as shown in Fig. 3. Five constraint functions with different purposes are embedded to govern the optimization process. The functions g_1 and g_2 are to prevent the curved beams from intersecting each other. The functions g_3 and g_4 define the bound for the width of slender beams and the angles defining points C_{14}, C_{24}, respectively. The stress of the mechanism is required in the constraint g_5.

Table 1. *Formulation of a compliant constant torque mechanism optimization*

1. *Objective*:
– Minimize the variation of the torque follow Eq. (1)
2. *Design variables*:
– Control points: $C_{ij}(x, y)$ $(i = 1 \div 2, j = 0 \div 4)$
– In-plane thickness: w
– Angles: α_1, α_2
3. Constraints:
i. g_1: $C_{11}(x) < 0$;
ii. g_2: $C_{1j}(x) > C_{2j}(x)$ $(j = 0 \div 4)$
iii. g_3: $0.7 \le w \le 1.5$ (mm)
iv. g_4: $\pi/18 \le \alpha \le \pi/1.5$ (rad)
v. The maximum stress within the CTM, g_5: $\sigma_m < \sigma_y/SF$

3. Results and Discussion

The designed CTM suffers a large deformation, so choosing a proper material plays a vital role. In this model, PEEK (polyether etherketone) is selected because of the large ratio σ_y/E. This ratio is often used to measure the ability of a material to allow bending before yield. For the linear elastic and isotropic model, the Young's modulus (E) of PEEK is taken as 3.58 GPa, the Poisson's ratio (v_p) is taken as 0.3, and the out-of-plane thickness of the structure is 5.0 mm.

Table 2. *Optimum DVs of the CTM*

Design variables	Values (mm)
$C_{10}(x, y)$	(0.00, 48.00)
$C_{11}(x, y)$	(-0.90, 25.47)
$C_{12}(x, y)$	(1.00, 32.53)
$C_{13}(x, y)$	(1.79, 32.53)
$C_{14}(x, y)$	(9.62, -2.74)
$C_{20}(x, y)$	(12.70, 58.13)
$C_{21}(x, y)$	(35.23, 58.13)
$C_{22}(x, y)$	(12.70, 35.60)
$C_{23}(x, y)$	(43.03, 15.90)
$C_{24}(x, y)$	(7.42, 22.83)
α_1	105.88°
α_2	18.00°
w	0.80

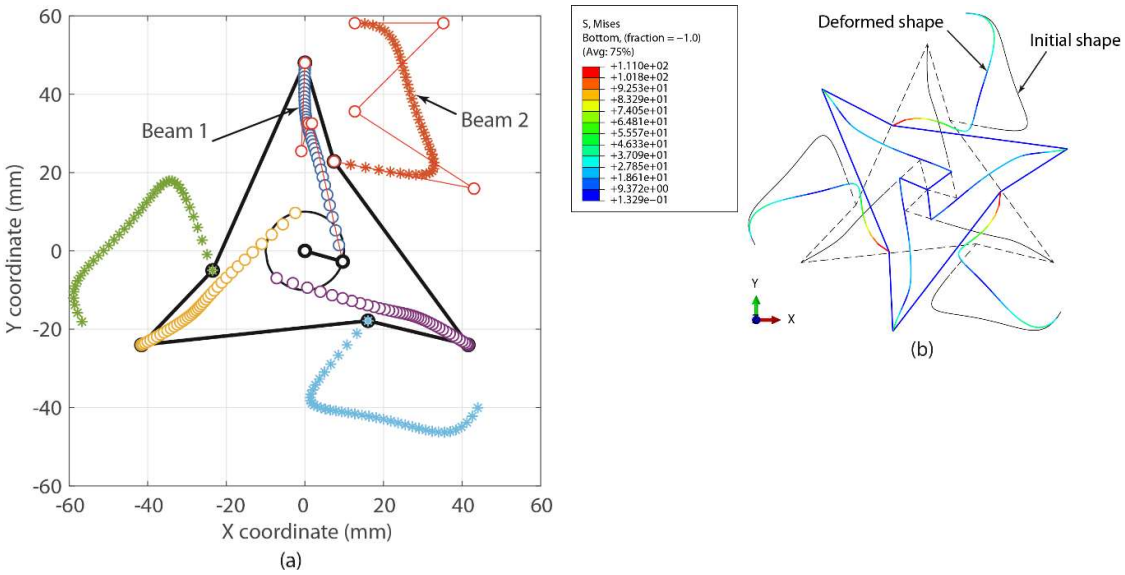

Fig. 5 - *FEM beam element model (a) and simulation results (b)*

The GA optimizations in MATLAB integrated with the FEA by ABAQUS are run with 30 generations and a population size of 40 candidates for each generation. The score is the optimal configurations of the proposed beam-based CTM shown in Fig. 5. These Bezier curved beams are created from the results of optimum design variables presented in Table 2. It is necessary to build a

three-dimension model to verify for the nonlinear stiffness and structural integrity of the mechanism and it is shown in Fig. 6. As seen in the Fig. 6, compliant members was structured in two floors to get enough space for the deformation to 110^0. In the 3D simulation, the anchor ring was eliminated to reduce the computational time.

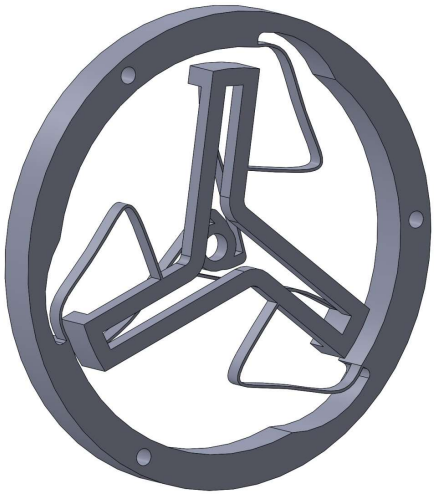

Fig. 6 - *3D model of the CTM*

The torque – rotation curves of the optimum mechanism are indicated in Fig. 7. In this research, both beam element model (2D) and solid model (3D) are used to analyze the mechanical behavior of the mechanism. The former model is used during the optimization stage to fasten the evaluation of a design due to its simplicity. However, the tradeoff of this method is the approximated modelling to the real mechanism. It is advisable that the latter 3D-simulation should be implemented to verify the final results. Fig. 7 shows that the constant-torque value of 3D model is slightly higher than that of 2D model. But they are in good agreement of both cases. The constant-torque range is divided into two stages at the angle of 58^o. The deviations of output torque of the CTM in the whole working range from 30^o to 110^o are 3.8% and 4.3% for 2D-beam model and 3D model, respectively, depicted in Table 3. The flatness of the torque curve between the operational ranges can be further improved by GA optimization algorithm if the generation evolution is extended. However, depending on the diversification of the initial population, global optimum solution in GA can also be hardly found if the whole generation are attracted to the local optima. The probability percentage of the two genetic operators in GA, crossover and mutation, can be intervened. Increasing the mutation possibility to produce more outsiders is one of the solutions to escape those local traps. In the current research, the variation of the torque between the working range is within the acceptable limits. Therefore, the evolution process is terminated after 30 generations. The torque can be adjusted to higher value by increasing the out-of-plane thickness without changing the flatness of the mechanism. The maximum stress of the mechanism stands at 128.6 MPa, shown in Fig. 7, is much smaller than the yield strength of the PEEK material $(\sigma_y = 210MPa)$. The stack-up configuration of the CTM introduces more challenges for the conventional fabrication methods. However with the rapid advancement of 3D-printing technology, the manufacturing for such kind of products becomes much easier than ever. For PEEK material, several feasible printing methods are fused filament fabrication (FFF), stereolithography (SLA) or selective laser sintering (SLS). In 3D-printing technology, the accuracy for each method is evaluated by two criteria, namely, trueness and precision according to the ISO 5725-1:1994/COR 1:1998. Msallem et al. [25] showed that SLS has the highest trueness (0.11 ± 0.016 mm) when they printed the anatomical models for clinical application. This method will be used to print the current mechanism and will be presented in the next research.

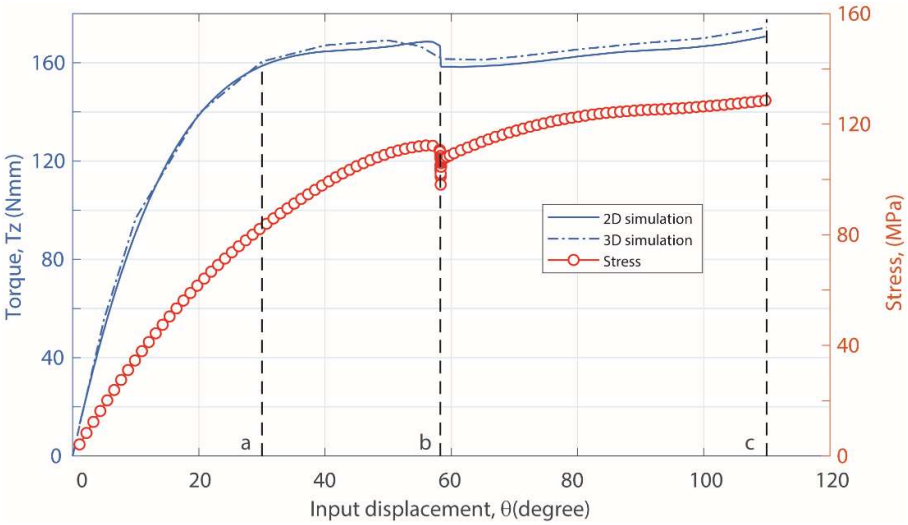

Fig. 7 - *Torque and stress – rotation results using FEA analysis*

Table 3. *Output torque deviation*

Model	Average value (at 40°)	Minimum (at 30°)	Maximum (at 110°)	Maximum Deviation (%)
2D	164.5	158.6	170.8	3.8
3D	167.1	160.5	174.3	4.3

3. Conclusions

In this paper, a simple and efficient method for the design of a compliant CTM was presented. A novel large-stroke CTM was proposed by using serially connected curved beams that deform sequentially. The optimum design is obtained by using genetic algorithm optimization coupled with finite element analysis. The enlarged operation range diversifies the probable applications for this kind of mechanism. In addition, taking the merits of compliant mechanisms, the designed CTM is a perfect replacement for the conventional mechatronic force control system, especially in mobility devices. In spite of the imperfect result, the proposed configuration is a worthy suggestion for extending the torque-constant range of other works in the future.

Acknowledgments

This work belongs to the project grant No: T2020-17 funded by Ho Chi Minh City University of Technology and Education, Vietnam.

REFERENCES

[1] L. L. Howell, *Compliant mechanisms*. New York: Wiley, 2001.
[2] X. Zhang and Q. Xu, "Design and analysis of a 2-DOF compliant gripper with constant-force flexure mechanism," *Journal of Micro-Bio Robotics,* vol. 15, no. 1, pp. 31-42, 2019.
[3] X. Zhang and Q. Xu, "Design and testing of a novel 2-DOF compound constant-force parallel gripper," *Precision Engineering,* vol. 56, pp. 53-61, 2019.
[4] X. Zhang and Q. Xu, "Design and development of a new 3-DOF active-type constant-force compliant parallel stage," *Mechanism and Machine Theory,* vol. 140, pp. 654-665, 2019.
[5] Q. Xu, "Design of a large-stroke bistable mechanism for the application in constant-force micropositioning stage," *Journal of Mechanisms and Robotics,* vol. 9, p. 7, 2017.
[6] G. W. Xiaozhi Zhang, Qingsong Xu "Design, Analysis and testing of a new compliant compound constant-force mechanism " *Actuators,* vol. 7, no. 4, 2018.
[7] D.-A. Wang, J.-H. Chen, and H.-T. Pham, "A constant-force bistable micromechanism," *Sensors and Actuators A: Physical,* vol. 189, pp. 481-487, 2013.
[8] C.-C. Lan, "A constant-force compliant gripper for handling objects of various sizes," *Journal of Mechanical Design,* vol. 136, p. 10, 2014.
[9] H.-T. Pham and D.-A. Wang, "A constant-force bistable mechanism for force regulation and overload protection," *Mechanism and Machine Theory,* vol. 46, p. 11, 2011.

[10] H.-T. Pham and N. H. N. Hieu, "Shape optimization and fabrication of a compliant constant - force mechanism," *Tạp chí Khoa học và Công nghệ,* vol. 115, p. 6, 2016.
[11] Y.-H. Chen and C.-C. Lan, "An adjustable constant-force mechanism for adaptive end-effector operations," *Journal of Mechanical Design,* vol. 134, no. 3, 2012.
[12] P. Bilancia and G. Berselli, "Design and testing of a monolithic compliant constant force mechanism," *Smart Materials and Structures,* vol. 29, no. 4, p. 044001, 2020.
[13] D. Nguyen, T.-V. Phan, and H.-T. Pham, "Design and analysis of a compliant gripper integrated with constant-force and static balanced mechanism for micro manipulation," in *2018 4th International Conference on Green Technology and Sustainable Development (GTSD)*, 2018, pp. 291-295.
[14] R. R. Torrealba, S. B. Udelman, and E. D. Fonseca-Rojas, "Design of variable impedance actuator for knee joint of a portable human gait rehabilitation exoskeleton," *Mechanism and Machine Theory,* vol. 116, pp. 248-261, 2017.
[15] Q. Liu *et al.*, "Development of a new robotic ankle rehabilitation platform for hemiplegic patients after stroke," *Journal of Healthcare Engineering,* vol. 2018, 2018.
[16] F. Sup, A. Bohara, and M. Goldfarb, "Design and control of a powered transfemoral prosthesis," *The International Journal of Robotics Research,* vol. 27, no. 2, pp. 263-273, 2008.
[17] H. Aguilar-Sierra, W. Yu, S. Salazar, and R. Lopez, "Design and control of hybrid actuation lower limb exoskeleton," *Advances in Mechanical Engineering,* vol. 7, no. 6, 2015.
[18] C.-W. Hou and C.-C. Lan, "Functional joint mechanisms with constant-torque outputs," *Mechanism and Machine Theory,* vol. 62, pp. 166-181, 2013/04/01/ 2013.
[19] J. McGuire, "Analysis and design of constant-torque springs used in aerospace applications," PhD. Dissertation, The University of Texas at Austin, 1994.
[20] H. Nair Prakashah and H. Zhou, "Synthesis of constant torque compliant mechanisms," *Journal of Mechanisms and Robotics,* vol. 8, no. 6, 2016.
[21] P. Wang, S. Yang, and Q. Xu, "Design and optimization of a new compliant rotary positioning stage with constant output torque," *International Journal of Precision Engineering and Manufacturing,* vol. 19, no. 12, pp. 1843-1850, 2018/12/01 2018.
[22] T.-V. Phan, and H.-T. Pham, and a. C.-N. Truong, "Design and analysis of a compliant constant-torque mechanism for rehabilitation devices," *In: Parinov I., Chang SH., Long B. (eds) Advanced Materials. Springer Proceedings in Materials,* vol. vol 6. Springer, Cham, p. 9, 2020.
[23] I. Gandhi and H. Zhou, "Synthesizing constant torque compliant mechanisms using precompressed beams," *Journal of Mechanical Design,* vol. 141, no. 1, 2018.
[24] P. Bilancia, S. P. Smith, G. Berselli, S. P. Magleby, and L. L. Howell, "Zero torque compliant mechanisms employing pre-buckled beams," *Journal of Mechanical Design,* vol. 142, no. 11, 2020.
[25] Msallem, N. Sharma, S. Cao, F. S. Halbeisen, H.-F. Zeilhofer, and F. M. Thieringer, "Evaluation of the Dimensional Accuracy of 3D-Printed Anatomical Mandibular Models Using FFF, SLA, SLS, MJ, and BJ Printing Technology," *Journal of Clinical Medicine,* vol. 9, no. 3, 2020.

Thanh-Vu Phan received the M.S. degree in mechanical engineering from Ho Chi Minh City University of Technology and Education, Vietnam, in 2012. He is currently pursuing the Ph.D. degree in mechanical engineering at Ho Chi Minh City University of Technology and Education, Vietnam. His research interest includes compliant mechanisms and advanced manufacturing

Huy-Tuan Pham received the Ph.D. degree in precision engineering from National Chung Hsing University, Taiwan in 2011. He is currently an Associate Professor at Ho Chi Minh City University of Technology and Education, Vietnam. His research interest includes compliant mechanisms and their applications, ultrasonics and vibration-assisted machining methods.

BỘ KHOA HỌC VÀ CÔNG NGHỆ
CỤC SỞ HỮU TRÍ TUỆ

CỘNG HOÀ XÃ HỘI CHỦ NGHĨA VIỆT NAM
Độc lập - Tự do - Hạnh phúc

Số: 260596/QĐ-SHTT.IP

Hà Nội, ngày 20 tháng 11 năm 2025

QUYẾT ĐỊNH
Về việc chấp nhận đơn hợp lệ

CỤC SỞ HỮU TRÍ TUỆ

Căn cứ Quyết định số 156/QĐ-BKHCN ngày 03/3/2025 của Bộ trưởng Bộ Khoa học và Công nghệ quy định chức năng, nhiệm vụ, quyền hạn và cơ cấu tổ chức của Cục Sở hữu trí tuệ;

Căn cứ khoản 4 Điều 109 của Luật Sở hữu trí tuệ ngày 29/11/2005, được sửa đổi, bổ sung theo Luật sửa đổi, bổ sung một số điều của Luật Sở hữu trí tuệ ngày 19/6/2009, Luật sửa đổi, bổ sung một số điều của Luật kinh doanh bảo hiểm, Luật Sở hữu trí tuệ ngày 14/6/2019 và Luật sửa đổi, bổ sung một số điều của Luật Sở hữu trí tuệ ngày 16/6/2022 (sau đây gọi tắt là Luật Sở hữu trí tuệ);

Căn cứ kết quả thẩm định hình thức đơn đăng ký sáng chế:

Số đơn: 1-2025-08416;

Theo đề nghị của Giám đốc Trung tâm Thẩm định Sáng chế.

QUYẾT ĐỊNH:

Điều 1. Chấp nhận đơn hợp lệ về hình thức với những ghi nhận sau đây:
Số đơn: 1-2025-08416 Ngày nộp đơn: 05/11/2025
Người nộp đơn(*): Trường Đại học sư phạm kỹ thuật thành phố Hồ Chí Minh (VN)
Địa chỉ: Số 1 Võ Văn Ngân, phường Thủ Đức, thành phố Hồ Chí Minh
Tên sáng chế: Thiết bị hỗ trợ chức năng khớp gối tích hợp cơ cấu đàn hồi ổn định mô-men

Điều 2. Công bố đơn trên Công báo Sở hữu công nghiệp theo quy định tại khoản 2 Điều 110 và thẩm định nội dung để đánh giá khả năng cấp văn bằng bảo hộ trong trường hợp có yêu cầu theo quy định tại điểm a khoản 1 Điều 114 của Luật Sở hữu trí tuệ.

Điều 3. Quyết định này có hiệu lực kể từ ngày ký. Chánh Văn phòng Cục, Trưởng phòng Đăng ký, Giám đốc Trung tâm Thẩm định Sáng chế và Giám đốc Trung tâm Thông tin sở hữu công nghiệp chịu trách nhiệm thi hành Quyết định này./.

Nơi nhận:
- Như Điều 3;
- Người nộp đơn;
- Lưu: VT, HS.

KT. CỤC TRƯỞNG
PHÓ CỤC TRƯỞNG

Lê Huy Anh

(*) Trong trường hợp đơn có nhiều người nộp đơn, đây là người nộp đơn thứ nhất ghi trong danh sách các người nộp đơn.